



Kent Academic Repository

Hicks, L. J., MacArthur, J. L., Bridges, J. C., Price, M. C., Wickham-Eade, Jamie E., Burchell, M. J., Hansford, G. M., Butterworth, A. L., Gurman, S. J. and Baker, S. H. (2017) *Magnetite in Comet Wild 2: Evidence for parent body aqueous alteration*. *Meteoritics & Planetary Science*, 52 (10). pp. 2075-2096. ISSN 1086-9379.

Downloaded from

<https://kar.kent.ac.uk/66873/> The University of Kent's Academic Repository KAR

The version of record is available from

<https://doi.org/10.1111/maps.12909>

This document version

Publisher pdf

DOI for this version

Licence for this version

CC BY (Attribution)

Additional information

Versions of research works

Versions of Record

If this version is the version of record, it is the same as the published version available on the publisher's web site. Cite as the published version.


Author Accepted Manuscripts

If this document is identified as the Author Accepted Manuscript it is the version after peer review but before type setting, copy editing or publisher branding. Cite as Surname, Initial. (Year) 'Title of article'. To be published in *Title of Journal*, Volume and issue numbers [peer-reviewed accepted version]. Available at: DOI or URL (Accessed: date).

Enquiries

If you have questions about this document contact ResearchSupport@kent.ac.uk. Please include the URL of the record in KAR. If you believe that your, or a third party's rights have been compromised through this document please see our [Take Down policy](https://www.kent.ac.uk/guides/kar-the-kent-academic-repository#policies) (available from <https://www.kent.ac.uk/guides/kar-the-kent-academic-repository#policies>).

Magnetite in comet Wild 2: Evidence for parent body aqueous alteration

L. J. HICKS^{1,*} , J. L. MACARTHUR¹, J. C. BRIDGES¹, M. C. PRICE², J. E. WICKHAM-EADE²,
M. J. BURCHELL², G. M. HANSFORD¹, A. L. BUTTERWORTH³, S. J. GURMAN⁴, and
S. H. BAKER⁴

¹Department of Physics & Astronomy, Space Research Centre, University of Leicester, Leicester LE1 7RH, UK

²School of Physical Sciences, University of Kent, Canterbury CT2 7NH, UK

³Space Sciences Laboratory, University of California at Berkeley, Berkeley, California 94720, USA

⁴Department of Physics & Astronomy, University of Leicester, Leicester LE1 7RH, UK

*Corresponding author. E-mail: ljh47@le.ac.uk

(Received 07 October 2016; revision accepted 15 May 2017)

Abstract—The mineralogy of comet 81P/Wild 2 particles, collected in aerogel by the Stardust mission, has been determined using synchrotron Fe-K X-ray absorption spectroscopy with in situ transmission XRD and X-ray fluorescence, plus complementary microRaman analyses. Our investigation focuses on the terminal grains of eight Stardust tracks: C2112,4,170,0,0; C2045,2,176,0,0; C2045,3,177,0,0; C2045,4,178,0,0; C2065,4,187,0,0; C2098,4,188,0,0; C2119,4,189,0,0; and C2119,5,190,0,0. Three terminal grains have been identified as near pure magnetite Fe₃O₄. The presence of magnetite shows affinities between the Wild 2 mineral assemblage and carbonaceous chondrites, and probably resulted from hydrothermal alteration of the coexisting FeNi and ferromagnesian silicates in the cometary parent body. In order to further explore this hypothesis, powdered material from a CR2 meteorite (NWA 10256) was shot into the aerogel at 6.1 km s⁻¹, using a light-gas gun, and keystones were then prepared in the same way as the Stardust keystones. Using similar analysis techniques to the eight Stardust tracks, a CR2 magnetite terminal grain establishes the likelihood of preserving magnetite during capture in silica aerogel.

INTRODUCTION

The NASA Stardust spacecraft returned to Earth in 2006, after having collected cometary material from the Jupiter-family comet 81P/Wild 2 in 2004 (Brownlee et al. 2006). From optical microscopy, it is estimated that the Stardust spacecraft collected thousands of cometary dust particles, 1–300 μm in size, totaling an estimated $\sim 3 \times 10^{-4}$ g in mass (Hörz et al. 2006; Burchell et al. 2008). The cometary material impacted at 6.1 km s⁻¹, and thousands of tracks exist within the retrieved silica aerogel cells containing the particles (only a few measuring >100 μm) at the terminal positions and along the track walls, which have been dissected using precision cutting techniques (Westphal et al. 2002). Aerogel and its use to capture dust in space in general is reviewed in Burchell et al. (2006a). For Stardust data, Burchell et al. (2008) visually classified the first 186 harvested tracks into three track types

based on their morphology. The narrow “carrot-shaped” type A tracks, which are dominated by single terminal particles, are found to be 86% of the total number of tracks. The more bulbous type B tracks have one terminal particle in 50% of those tracks, two in nearly one-third of those tracks, and 21% of type B tracks have three or more terminal particles. Burchell et al. (2008) suggested that type A particles are stronger materials, well consolidated into usually a single, volatile-poor grain, for example, either olivine, pyroxene, or chondrule fragments, etc. Type B grains are either more loosely bound or more volatile rich, and were more readily disrupted into fragments during capture (Trigo-Rodríguez et al. 2008). As well as mechanical fragmentation of grains arising from shock pressures of up to 800 MPa (Trigo-Rodríguez et al. 2008), which is well above the strength of many dust assemblages, the aerogel capture process can also introduce a heat pulse to the grains. This heat pulse is of short duration but can

exceed 1000 K (e.g., see Noguchi et al. [2007], who reported heating effects of over 500 °C on grain surfaces on the order of 1 microsecond). For larger terminal grains this can have a minimal effect, but for finer grained material from particularly type B tracks this can induce some material processing when the small grains can effectively gain a molten aerogel wrap (Leroux 2012). Surface material can be lost from grains via ablation, and organic components may be particularly prone to this (Burchell et al. 2009).

Initial investigations of aerogel tracks found the cometary material to be crystalline and consist largely of ferromagnesian silicates, olivines, and pyroxenes, having formed at high temperatures (Zolensky et al. 2006). Additional constituents include fragments of calcium-aluminum-rich inclusions (CAIs) (Simon et al. 2008; Matzel et al. 2010), and chondrule-like fragments including ferromagnesian and Al-rich compositions (Nakamura et al. 2008; Bridges et al. 2012; Ogliore et al. 2012; Joswiak et al. 2014). Many of these reports suggest links between carbonaceous chondrites and the Wild 2 material.

Using X-ray absorption spectroscopy (XAS), transmission electron microscopy (TEM), scanning transmission X-ray microscopy (STXM), and Raman techniques, Fe-oxide minerals have been identified in the Stardust tracks. These oxides include magnetite (Fe_3O_4) and some hematite (Fe_2O_3) present as subgrain material along the walls of type A and B tracks (Bridges et al. 2010; Changela et al. 2012; Stodolna et al. 2012a) and a possible Cr-rich magnetite terminal grain (De Gregorio et al. 2015).

Magnetite grains are prominent in carbonaceous chondrites, if they have been oxidized and aqueously altered (Brearley and Jones 1998; Hutchison 2004; Weisberg et al. 2006). For instance, it is present in CI chondrites as the second most abundant phase, and is also abundant in CR and CV chondrites, in fine-grained chondrule rims of fayalite-hedenbergite-magnetite assemblages in CM chondrites, but is typically absent from CO chondrites (Choi et al. 1997; Krot et al. 2000; Brearley 2006). Kerridge (1970) and Kerridge et al. (1979) proposed that framboidal magnetites in the CII chondrite Orgueil were the result of oxidation and low-temperature alteration of FeMg-rich silicates, requiring aqueous activity in the meteorite parent body. Hematite and maghemite $\gamma\text{-Fe}_2\text{O}_3$ are other Fe oxides present in chondrites, but in minor or trace amounts. This makes magnetite an important mineral to identify and study in Wild 2 samples because it is often interpreted as a tracer for parent body water–rock reactions. Parent body aqueous alteration has also been suggested by Berger et al. (2011), based on the presence of cubanite (CuFe_2S_3) in Comet Wild 2, and by analogy with

Orgueil. However, the record of hydrous alteration in Stardust grains remains uncertain, with the nondetection of phyllosilicate being interpreted as evidence for a lack of hydrous alteration (Westphal et al. 2017).

In order to obtain accurate information about Comet Wild 2 minerals and their environment of formation, this paper focuses on the terminal grains of eight newly harvested tracks, six of which are type B tracks and the others type A. The focus on relatively larger terminal particles, for example, $>10\ \mu\text{m}$, is because they are grains that have remained primarily intact and unaltered as they impacted the aerogel.

In addition to studying aerogel keystones from the Stardust collection, powdered carbonaceous chondrite material, shot into the aerogel using a light-gas gun, was also investigated by preparing and analyzing the samples using the same techniques as the Stardust keystones. Here, we look at powdered material from a CR2 chondrite meteorite, selected as an analogue to Wild 2, including the presence of magnetite grains, chondrules, and CAIs (Hutchison 2004; Weisberg et al. 2006). The results aid in testing the hypothesis that the magnetite grains found in Stardust tracks, along with FeNi and ferromagnesian silicates, CAIs, and chondrule-like fragments, are revealing many affinities between Wild 2 and carbonaceous chondrites. In particular, our work focuses on the characterization of Fe oxides in order to reveal information about a record of potential aqueous alteration.

METHODS AND SAMPLES

Eight impact tracks in seven Stardust keystones have been investigated (listed in order of track number): C2112,4,170,0,0 (#170); C2045,2,176,0,0 (#176); C2045,3,177,0,0 (#177); C2045,4,178,0,0 (#178); C2065,4,187,0,0 (#187); C2098,4,188,0,0 (#188); C2119,4,189,0,0 (#189); and C2119,5,190,0,0 (#190). In the work below we refer to tracks by the nomenclature #nnn. Regarding the Stardust sample nomenclature, the full track number refers to Stardust tray “C2” used on the mission to collect cometary samples, followed by the individual aerogel cell number (000-132), and the keystone subdivision of each cell to find the track. The track numbers (e.g., #170) are listed in order, as they are harvested and recorded. The latter two numbers are further subdivisions for that particular track. Optical microscope images of each track are presented in Fig. 1.

I-18 Beamline (Diamond Light Source synchrotron)

Using the I-18 Beamline, of the Diamond Light Source synchrotron, Oxfordshire, UK, we have

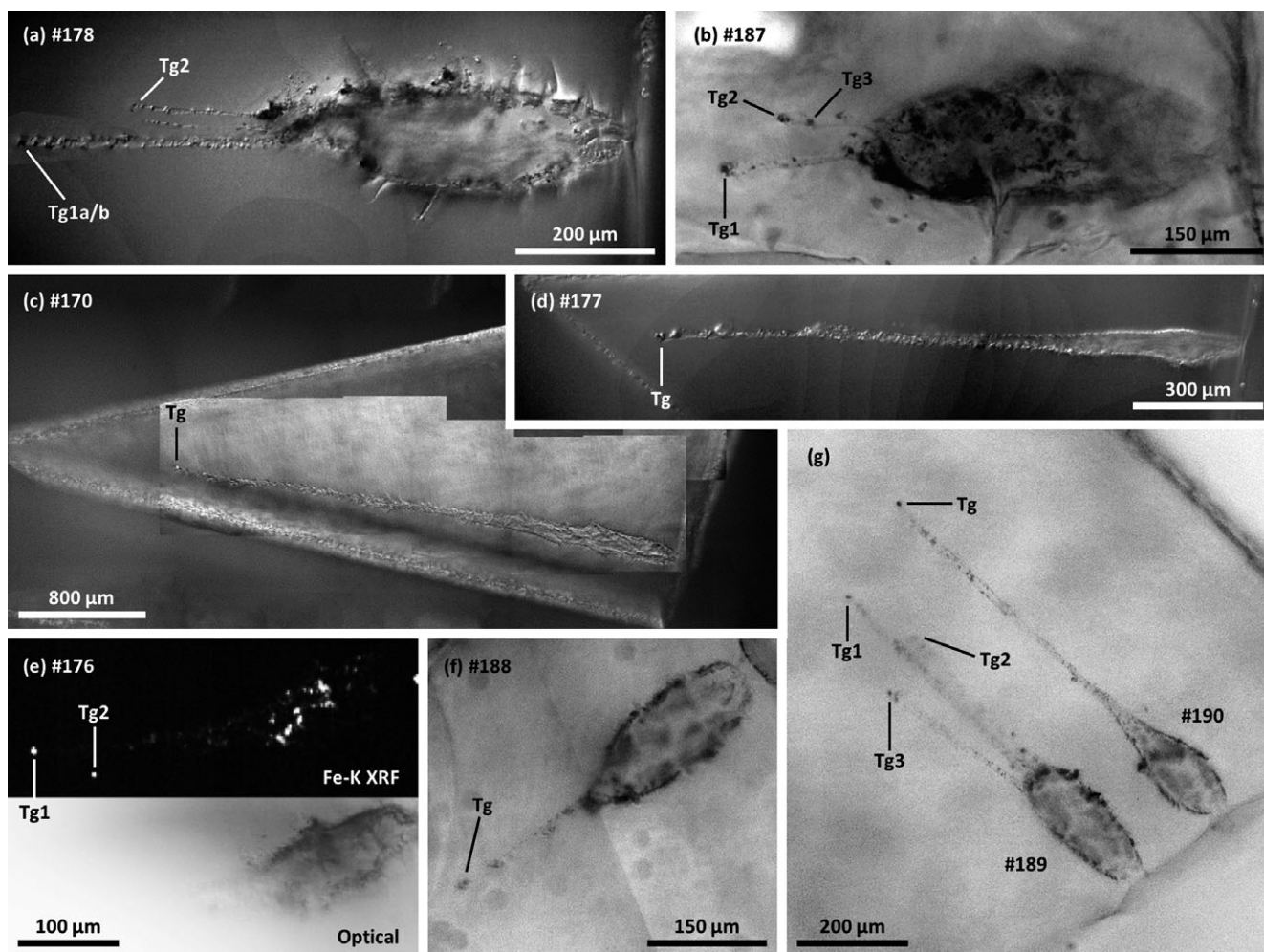


Fig. 1. Optical microscope images of each of the seven Stardust aerogel keystones and eight tracks investigated in this paper, plus one Fe-K XRF map of track #176. a) Track #178: a Type B track, 0.9 mm in length with at least two styli featuring terminal grains (Tg1 and Tg2). The main stylus contains two terminal grains, separated by $\sim 10 \mu\text{m}$, referred to as Tg1a and Tg1b, which consist of magnetite and olivine, respectively. Terminal grain Tg2 is magnetite. b) Track #187: a Type B track, 0.59 mm in length, with at least two styli featuring three terminal grains, consisting of magnetite (Tg1), olivine (Tg2), and troilite (Tg3). c) #170: a Type A track, measuring 3.2 mm in length, featuring a $\sim 20 \mu\text{m}$ terminal grain (Tg) consisting of Fe-metal and Cr-bearing silicate, plus hematite in the subgrain near the track entrance. d) Track #177: a Type A track, measuring 1.35 mm in length, with a terminal grain (Tg) consisting of Cr-bearing olivine. e) #176: a Type B track, measuring 380 μm in length, with at least two styli featuring a terminal grain each, consisting of Fe-Ni-metal (Tg1) and Fe-metal (Tg2). There was difficulty in imaging track #176 with an optical microscope, but an XRF map was produced of the entire track, revealing the terminal grains and subgrain material. f) Track #188: a Type B track, measuring 460 μm in length, featuring one stylus with a terminal grain (Tg) consisting of troilite. g) Track #189 (left) and #190 (right): two Type B tracks within in the same keystone. Track #189 measures 740 μm in length, featuring at least three styli and terminal grain each, consisting of an uncertain mineralogy but possibly magnetite (Tg1), and pyroxene (Tg3). Locating terminal grain Tg2 was unsuccessful. Track #190 measures 810 μm featuring one stylus and terminal grain (Tg) consisting of pyroxene.

analyzed grains with X-ray fluorescence (XRF), XAS including the X-ray absorption near-edge structure (XANES), extended X-ray absorption fine structure (EXAFS) features, and transmission X-ray diffraction (XRD). The beamline has an energy range of 2.0–20.7 keV, measuring K-edges for elements P ($Z = 15$) to Mo ($Z = 42$), with a spot size capability reduced to a spatial resolution of $\sim 2 \times 2.5 \mu\text{m}$. The tuneable

monochromators are capable of resolving small spectral energy increments of $\sim 0.1 \text{ eV}$ (Mosselmans et al. 2009).

X-ray Fluorescence

X-ray fluorescence on the I-18 Beamline can be used to produce elemental maps, measuring elements above Ca in atomic weight ($Z > 20$) using an incident X-ray beam between 8.5 and 9.0 keV, giving the

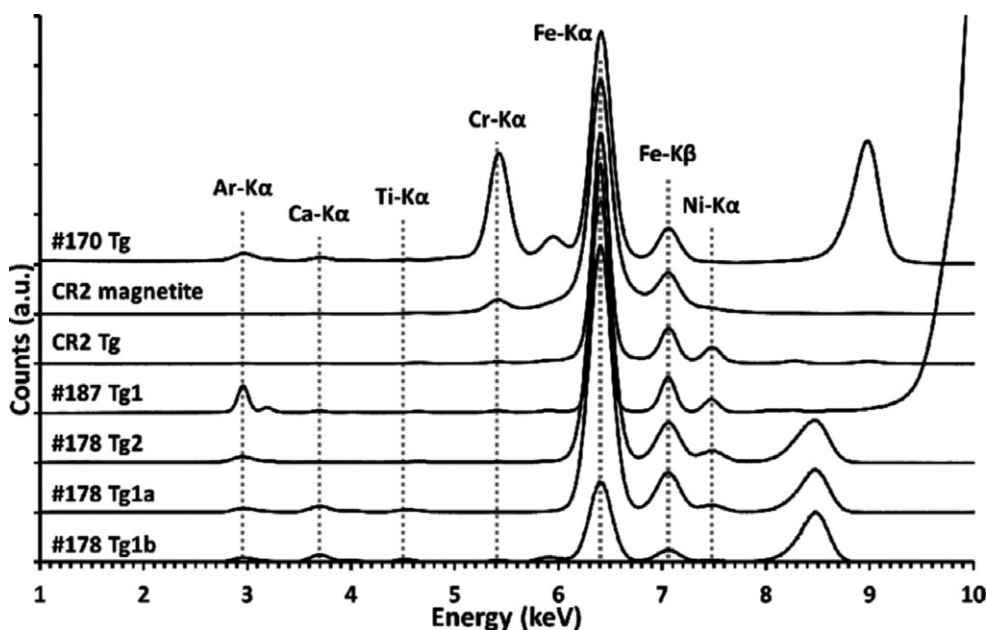


Fig. 2. XRF spectra of terminal grains. #170 Tg is a Fe-metal grain with a Cr-rich silicate phase. #178 Tg1a and Tg2 and #187 Tg1 have been identified as magnetite grains, all with a minor amount of Ni. For comparison the terminal grain #178 Tg1b, identified as an olivine grain, is part of the same terminal grain track as the magnetite (Tg1a), but both grains are separated by $\sim 10 \mu\text{m}$. XRF measurements of the aerogel surrounding the grains #178 Tg1a and Tg1b also revealed a minor Ca content and is possibly contamination. The analogue terminal grain sample of CR2 magnetite also shows the Fe-rich content with a minor phase of Ni, whereas the measurement of a magnetite grain from a thin section of the same CR2 meteorite shows a Fe-rich content with a trace of Cr. Peaks seen >8.5 are the Rayleigh scatter peaks due to the energy of the incident X-ray beam set for that particular measurement.

elemental distribution of K, Ca, Ti, Cr, Mn, Fe, and Ni, in the cometary material along the track in the aerogel. Maps of the tracks were used to locate terminal and subgrain material with $2 \mu\text{m}$ per pixel resolution images. The energy spectra of the terminal grains were analyzed using PyMca 4.4.1 and are presented in Fig. 2, with the chemical composition shown in Table 1.

Fe-K X-ray Absorption Spectroscopy

Fe-K X-ray absorption spectroscopy (Fe-K XAS) measurements were made in fluorescence and transmission modes. All Fe-K XAS measurements were taken over an energy range which varied, but typically ranged between 6900 eV and 7660 eV. This range covers the relevant spectral features for Fe-K XANES and EXAFS analysis. The energy resolution of the measurements were also set to vary throughout the range, with a significant focus of higher resolution of 0.1 eV increments over the XANES region 7090–7145 eV, followed by varying reduced energy resolution of 0.2–0.4 eV increments over the EXAFS region up to 7660 eV. The higher resolution of 0.1 eV over the XANES region is necessary to accurately determine and analyze the small (<5.0 eV) shifts and variations that occur in the $1s \rightarrow 3d$ transition pre-edge peak structure and the Fe-K absorption edge.

The normalized data have been processed using a code written specifically to use a spline function across the Fe-K $1s \rightarrow 3d$ peaks and compiled in IDL 8.5. Based on a similar method used in Berry et al. (2003) and Wilke et al. (2001), a curved spline function baseline is fitted under the $1s \rightarrow 3d$ peaks and subtracted from the spectra, from which an intensity-weighted average centroid energy position is estimated over these peaks. This centroid energy position can be used to assess the atomic configuration of the materials measured and estimate the oxidation state of Fe-silicates and Fe-oxides (Wilke et al. 2001; Berry et al. 2003; Bunker 2010; Hicks et al. 2014), with average percentage errors of 10.7% and 1.1%, for Fe-silicates and Fe-oxides, respectively, based on average centroid energy position values. Analyzing the Fe-K absorption edge can also be used to estimate the oxidation state, defined as the ionization threshold to the continuum states. The absorption edge position is taken as the energy of the XAS spectra at half normalized intensity. Both the Fe-K absorption edge and the $1s \rightarrow 3d$ pre-edge centroid are accurately determined to the nearest 0.05 eV.

To analyze the EXAFS, the Ifeffit-Athena normalized XAS data were processed and analyzed using PySpline 1.2, providing data suitable for analysis in

Table 1. Fe-K and Cr-K XAS analysis of cometary grains and CR2 analog samples, and reference materials.

Sample	Grain	Type/size	XRF detected composition	XAS type	XANES Fe-K absorption edge (± 0.05 eV)	XANES 1s \rightarrow 3d Centroid (± 0.05 eV)	Concluding mineral type
Stardust Tracks							
#170	Tg	20 μm	Fe-Cr-rich	Fe-K	7118.4	7113.0	Fe-metal
				Cr-K	5996.2	–	Cr-silicate
#176	Tg1	~ 5 μm	Fe-rich with Ni	Fe-K	7118.4	7112.9	Fe-metal ^a
	Tg2	~ 5 μm	Fe-rich	Fe-K	7117.7	7112.9	Fe-metal
#177	Tg	~ 4 μm	Fe-rich with Cr	Fe-K	7119.6	7112.5	Olivine
				Cr-K	5996.8	–	Cr-silicate
#178	Tg1a	10 μm	Fe-rich	Fe-K	7121.5	7113.1	Magnetite
	Tg1b	6 μm	Fe-rich	Fe-K	7120.2	7112.3	Olivine
	Tg2	~ 6 μm	Fe-rich				Magnetite
#187	Tg1	5 μm	Fe-rich	Fe-K	7121.0	7113.5	Magnetite
	Tg2	5 μm	Fe-rich	Fe-K	7119.2	7112.3	Olivine
	Tg3	~ 5 μm	Fe-rich with Ni	Fe-K	7117.0	7111.8	Fe-Ni-sulfide
#188	Tg	~ 5 μm	Fe-rich	Fe-K	7117.5	7111.7	Fe-sulfide
#189	Tg1	~ 7 μm	Fe-Ca-rich, with Mn	Fe-K	7121.1	7113.1	Magnetite ^a
	Tg3	~ 5 μm	Fe-rich	Fe-K	7119.4	7112.3	Pyroxene
#190	Tg	~ 7 μm	Fe-rich with Cr	Fe-K	7118.6	–	Pyroxene ^a
Analogue sample (NWA 10256)							
CR2	Tg	~ 30 μm	Fe-rich with Ni	Fe-K	7121.8	7113.1	Magnetite
CR2		Section	Fe-rich with Cr	Fe-K	7119.4	7113.0	Magnetite
Reference materials used							
Magnetite		Powder		Fe-K	7120.8	7113.2	Magnetite
Magnetite		Self-absorbing		Fe-K	7119.4	7113.1	Magnetite
Fe-metal		Foil		Fe-K	7121.9	7113.1	Fe-metal
Tuxtuac (LL5)		Section		Fe-K	7113.0		Taenite
San Carlos		Section		Fe-K	7119.4	7111.7	Olivine
Tuxtuac (LL5)		Section		Fe-K	7118.8	7111.9	Olivine
Barwell (L5)		Section		Fe-K	7118.7	7111.7	Olivine
Tuxtuac (LL5)		Section		Fe-K	7118.9	7112.1	Pyroxene
Augite		Powder		Fe-K	7119.2	7111.8	Pyroxene
Hematite		Powder		Fe-K	7123.0	7114.0	Hematite
Goethite		Powder		Fe-K	7122.2	7113.7	Goethite
Chromite		Powder		Fe-K	7121.1	7112.5	Chromite
Chromite		Powder		Cr-K	5999.4	–	Chromite
JP-1		Powder		Fe-K	7119.3	7112.1	Pyrrhotite
Pyrrhotite		Powder		Fe-K	7116.7	7112.0	Pyrrhotite
Tuxtuac (LL5)		Section		Fe-K	7116.0	7111.8	Troilite
IMt-1		Powder		Fe-K	7122.8	7113.3	Illite
BM1972,142		Powder		Fe-K	7123.0	7113.1	Nontronite
NG-1		Powder		Fe-K	7123.9	7113.2	Nontronite
NAu-2		Powder		Fe-K	7123.9	7113.2	Nontronite
Tuxtuac (LL5)		Section		Fe-K	7116.4	7111.7	Pentlandite

^aThere is uncertainty in the identification of this grain due to a lack of good comparisons with reference materials.

DL_EXCURV v1.01 (Roy and Gurman 2001; Tomić et al. 2004). The results of this analysis reveal the bond lengths of neighboring atoms, such as O and Si, to the Fe atoms with which the beam interacts, as well as the ferric proportion ($\text{Fe}^{3+}/\Sigma\text{Fe}$) of the cometary grains. Error values are determined based on the resultant mean square relative displacement values and an amplitude reduction factor of $S^2_0 = 0.7$ was used for all analyses.

All of the Fe-K XAS analyses and results presented here are from measurements using the I-18 Beamline at Diamond Light Source. However, the measurements were performed during four separate beamtime sessions in December 2011 (#170), December 2013 (#176, #177, and #178), December 2014 (#187, #188, #189, and #190), and July 2016 (CR2 chondrite). Between each beamtime, some drift in the monochromators is

expected and an energy calibration is required (Kraft et al. 1996). Therefore, reference materials such as Fe-metal foil, and powdered magnetite ($\text{Fe}^{2+}\text{Fe}_2^{3+}\text{O}_4$), hematite ($\text{Fe}_2^{3+}\text{O}_3$), and San Carlos olivine ($[\text{Fe}^{2+}\text{Mg}^{2+}]_2\text{SiO}_4$; $\text{Fo}_{90.7}$) were measured at each beamtime, determining their Fe-K $1s \rightarrow 3d$ pre-edge centroid and absorption edge positions, to estimate the energy variation between each beamtime. These standards are also used as reference materials to compare with the cometary samples. Between the four beamtime sessions the energy has been estimated to have drifted by as much as 2.5 eV, thus adjusting all the results to the current (most recent) energy calibration was essential in order to observe the ~ 0.1 eV variations in the Fe-K XANES between samples.

The raw data for all Fe-K XAS measurements have been processed and normalized using Athena 0.8.056, and all final results for cometary and meteorite samples and reference materials, including Fe-K XAS estimations of the $1s \rightarrow 3d$ pre-edge centroid and Fe-K absorption edge position, are shown in Table 1.

Transmission XRD

Transmission XRD measurements of the terminal grains and some subgrain material were performed on all tracks. However, no XRD measurements were made of the terminal grain in #170, due to in situ XRD and XAS not being available at that time. The detector was set to receive transmission X-rays and capable of detecting and imaging 2θ angles ranging between $\sim 4^\circ$ and $\sim 40^\circ$. With a beam energy of 13 keV ($\lambda = 0.95 \text{ \AA}$), the available range corresponds to observing d -spacings approximately ranging between $\sim 1.4 \text{ \AA}$ and $\sim 9.1 \text{ \AA}$, and each measurement had an exposure time of 300 s. The XRD data were processed through IGOR Pro 6.22 (Wavemetrics) and/or DAWN 1.9 (Basham et al. 2015), and standards (magnetite, olivine, pyroxene, hematite, etc.) were also measured in “powder” form for calibration as reference material. Analyses of the results include comparisons to XRD measurements of the reference materials listed in Table 1, and d -spacing searches of the International Centre for Diffraction Data’s database (ICDD, 2015) and the American Mineralogical Crystal Structure Database (Downs and Hall-Wallace 2003).

MicroRaman Spectroscopy

The Stardust aerogel is largely transparent to the optical wavelengths typically used in Raman spectroscopy, making Raman spectroscopy important for complementary analyses of the grains captured in aerogel (Burchell et al. 2001, 2004, 2006b). Due to the potential damaging effects caused by laser heating in

Raman spectroscopy, initial analyses with the less destructive XAS and XRD methods were made before further investigation using Raman spectroscopy. All tracks were investigated at the University of Kent using a Horiba LabRam-HR Raman spectrometer, incorporating four lasers at 785 nm, 633 nm, 532 nm, and 473 nm. Because laser heating of samples is a potential problem (Hibbert and Price 2014), care was taken to use as low a laser power as possible to avoid damaging the grains. For the measurements reported here a 10% neutral density filter was used at all times, which limited the power at the sample (through a $\times 50$ objective) to a maximum of ~ 3 mW, thus avoiding unwanted heating and possible modification of the grain (De Faria et al. 1997).

CR2 Carbonaceous Chondrite Analogue

In this investigation we studied the NWA 10256 CR2 chondrite. Interior parts of the sample, away from the fusion crust, were ground into a powder with grain size 25–200 μm . The powders were fired into aerogel of density gradient 25–55 mg cm^{-3} at speeds of 6.1–6.3 km s^{-1} , similar to work reported in Burchell et al. (2008) using a two-stage light-gas gun (Burchell et al. 1999). This was necessary to approximately simulate the conditions experienced by the Stardust collected material. Keystones containing the CR2 impact tracks were prepared from the aerogel blocks using similar techniques to the keystones prepared from Stardust aerogel cells (Westphal et al. 2004). The terminal grains were investigated in the same way as the Stardust grains, acquiring measurements in Fe-K XAS, transmission XRD, and XRF. A polished thin section was also produced from the meteorite sample and characterized using a Phillips XL30 ESEM with Oxford INCA 350 EDX system. The same section was also analyzed with Fe-K XAS and XRF at the Diamond synchrotron.

The light-gas gun at the University of Kent successfully produced many tracks in aerogel from the powdered CR2 material, shot at 6.1 km s^{-1} . A keystone was then cut containing a track and $\sim 30 \mu\text{m}$ terminal grain (Fig. 3). The track was a type B track, but the bulbous region was removed during keystone preparation, with a track stylus measuring 650 μm long remaining in the keystone.

RESULTS

Terminal grains were identified, with sizes ranging between $\sim 4 \mu\text{m}$ and $\sim 20 \mu\text{m}$, using XRF mapping. Figure 1 shows a collection of optical microscope images for the eight tracks investigated, two of which



Fig. 3. A keystone with a NWA 10256 CR2 chondrite magnetite terminal grain, shot into aerogel at 6.10 km s^{-1} using the light-gas gun at the University of Kent (Burchell et al. 2008). The remaining track stylus cut from the aerogel, minus the bulbous region, measures $650 \mu\text{m}$ with a $\sim 30 \mu\text{m}$ terminal grain.

have a type A morphology (tracks #170 and #177), which suggest a robust mineral grain and cohesive impactor, possibly with a high proportion of high-temperature fragments (Burchell et al. 2008; Kearsley et al. 2012). The rest of the tracks (#176, #178, #187, #188, #189, and #190) have a type B track morphology, typically featuring more than one stylus, and feature solid terminal grains broken away from the original particle mass that impacted the Stardust aerogel. Therefore, where necessary for cataloging, the terminal grains identified in each track have been numbered (Tg1, Tg2, etc.) in order of stylus length from longest to shortest.

Magnetite

Magnetite was identified in at least two of the tracks: #178 and #187.

Track C2045,4,178,0,0 (#178)

Figure 1a shows track #178 to be a type B track, with a large bulbous region containing much subgrain residue material and several styli, measuring a total length of $950 \mu\text{m}$. There are at least two significant styli, extending beyond the bulbous part of the track, that feature terminal grains, and a third smaller stylus between the main two, but no terminal grain of significant size could be identified. The main stylus contains two terminal grains separated by $\sim 10 \mu\text{m}$, with the larger grain measuring $10 \mu\text{m}$ (Tg1a) and the smaller grain $6 \mu\text{m}$ (Tg1b). The second stylus contains a single $\sim 6 \mu\text{m}$ terminal grain (Tg2).

Analysis of the XRF measurements, shown in Fig. 2, found the two grains Tg1a and Tg2 to have a high concentration of Fe, plus a minor Ni presence. To a lesser extent, the smaller Tg1b grain is also Fe rich as evident from the spectrum shown in Fig. 2, but this grain also has trace Ni, Mn, and Cr. The minor Ca and

Ti content present in Tg1a and Tg1b was also observed in the aerogel immediately surrounding the grains ($>20 \mu\text{m}$ distant), but is not present in the aerogel surrounding Tg2 of the same #178 keystone, and is possibly contamination.

The Fe-K XAS presented in Fig. 4 shows similar spectra between the magnetite standard and Tg1a, with a near identical $1s \rightarrow 3d$ pre-edge centroid position at 7113.1 eV (see Table 1). However, the Fe-K absorption edge position at 7121.5 eV in Tg1a is 0.6 eV higher than that of the magnetite standard, suggesting a slightly higher oxidation state, between magnetite and hematite.

As shown in Fig. 5 and Table 2, the d -spacings measured in #178 Tg1a and Tg2 are a near identical match to the XRD measurement of a powdered magnetite standard. The varying intensities for each peak are to be expected when measuring such micron-sized grains due to incomplete powder averaging. The broadening of certain peaks may be due to microstructural imperfections and atomic disorder (Delhez et al. 1993), likely a result of strain in the sample where heating occurred during aerogel impact creating $<1 \mu\text{m}$ deep partially amorphous rim around the grains (Noguchi et al. 2007; Stodolna et al. 2012b).

There are minor discrepancies in the XRD d -spacing estimates with unit cell dimensions at 8.370 \AA and 8.357 \AA for Tg1a and Tg2, respectively, as they are less than the 8.387 \AA unit cell dimension measured in the powdered magnetite standard, or 8.396 \AA for the magnetite samples referenced in Table 2. Unit cell dimensions for maghemite ($\gamma\text{-Fe}_2^{3+}\text{O}_3$) at 8.330 \AA and trevorite ($\text{Ni}^{2+}\text{Fe}_2^{3+}\text{O}_4$) at 8.347 \AA and 8.363 \AA are also given in Table 2, both of which are minerals of the magnetite (iron spinel) series with similar crystal structures. A minor trevorite solid solution fraction within the Stardust magnetite grains, as suggested by the XRF detection of Ni traces (Fig. 2), may be

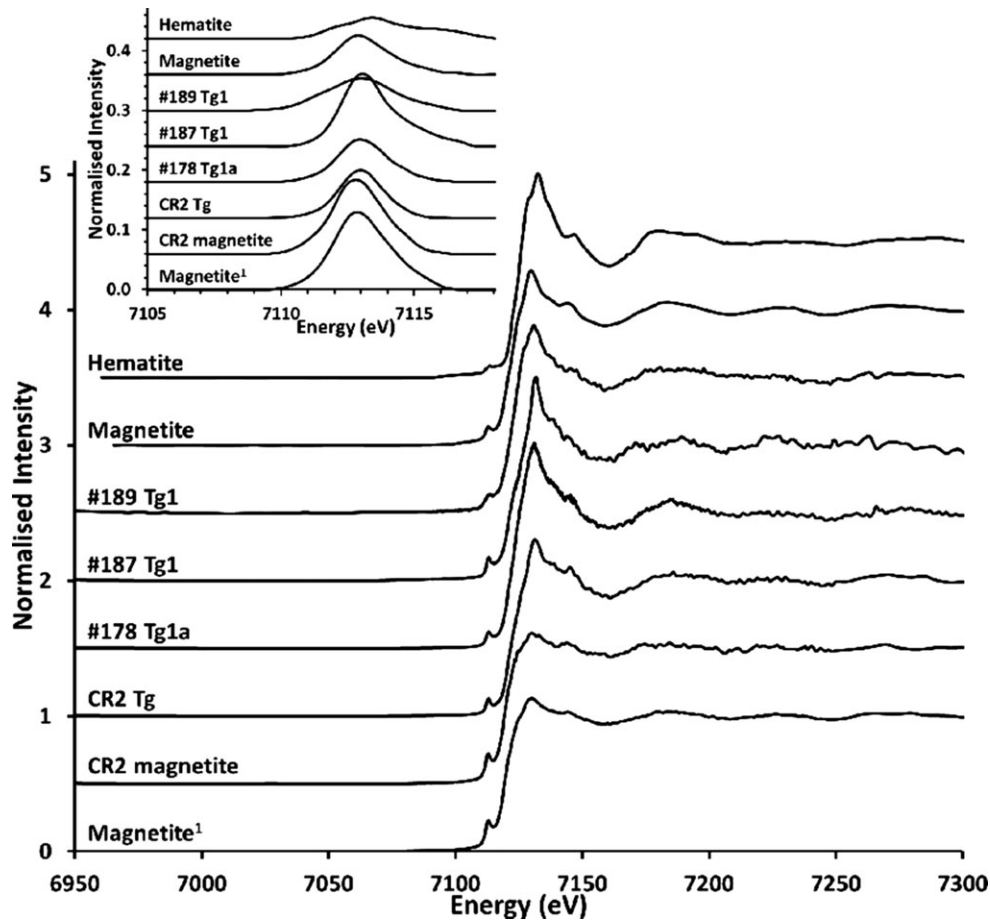


Fig. 4. The Fe-K XAS and pre-edge centroid of terminal grains in tracks #178 (Tg1a), #187 (Tg1), and #189 Tg1, and the analog CR2 terminal grain (Tg) shot into aerogel, compared to magnetite and hematite standard reference material. Each of the terminal grains show similarities to magnetite. The estimated energy values $1s \rightarrow 3d$ pre-edge centroid (see inset) and Fe-K absorption edge for the reference magnetite and cometary grains can be seen in Table 1. A thick and concentrated magnetite standard reveals the effects on XAS structure due to self-absorption in a sample, which shows similarities to the CR2 magnetite from a polished thin section.

responsible for the d -spacing discrepancy resulting in unit cell dimensions which deviate slightly from pure magnetite. Alternatively, a minor presence of maghemite due to oxidation of the magnetite could also explain the d -spacing discrepancy. As Ni in magnetite replaces the Fe^{2+} , both Ni replacement and/or oxidation would increase the ferric-ferrous ratio and cause a shift in the Fe-K XAS absorption edge position.

The smaller Tg1b grain has been identified as olivine based on the Fe-K XAS spectra (Fig. 6). The $1s \rightarrow 3d$ pre-edge centroid and Fe-K absorption edge positions, shown in Table 1 to be 7112.3 eV and 7120.2 eV, respectively, reveal a positive shift of nearly ~ 1 eV over that of the ferrous olivines in the Tuxtuac (LL5) and Barwell (L5) chondrites that we also analyzed. This suggests that the smaller terminal grain may have a minor ferric content of $\text{Fe}^{3+}/\Sigma\text{Fe} \leq 0.5$, based on the ferric-ferrous ratio estimations from Fe-K

$1s \rightarrow 3d$ analyses (Hicks et al. 2014). The Fe-K absorption edge of a more ferric material, such as magnetite, typically presents a further increased shift of ~ 1 eV or higher, compared to the absorption edge seen Tg1b, but a second mineral phase within this $6 \mu\text{m}$ sized grain influencing the overall XAS spectrum cannot be excluded.

Figure 7 shows Raman spectra measured for the #178 Tg1b terminal grain with two significant peaks detected at 821.7 cm^{-1} and 853.8 cm^{-1} . Using the equation given by Foster et al. (2013), the mineralogical composition of the olivine is determined from the positions of the two peaks, corresponding to a lower limit of Fo_{80} . The Mg-rich composition of this olivine would not have been determined by XRF measurements, as Mg is below the detection limits of the synchrotron beamline detector. When assigning a Fo content via Raman spectroscopy to particles

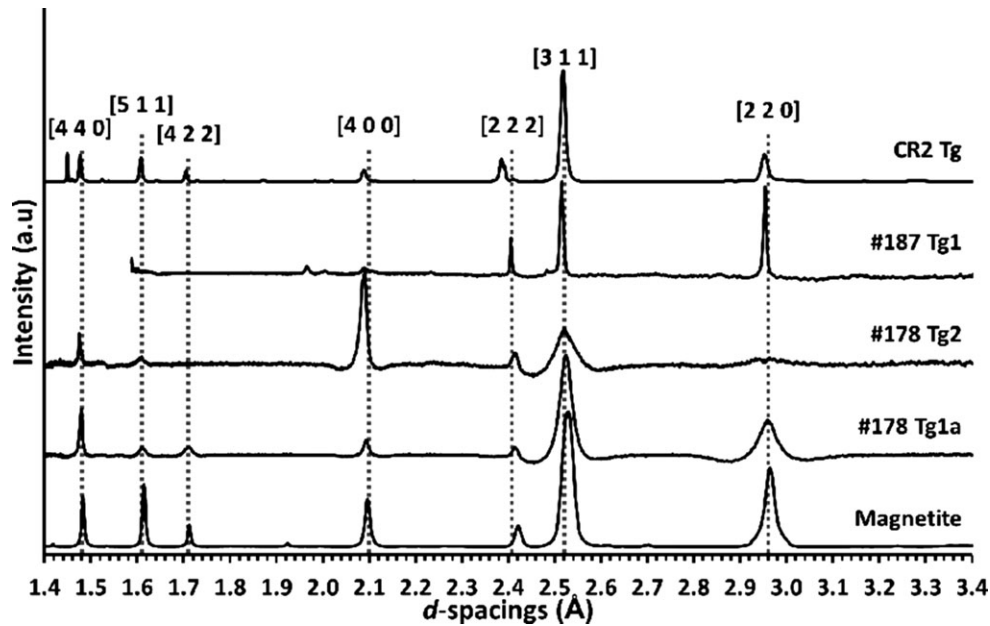


Fig. 5. XRD measurements for the larger terminal grains of #178 (Tg1a and Tg2), and from the terminal grain of #187 (Tg1). These are nearly identical to the measured powder magnetite standards and the aerogel shot CR2 terminal grain. The broad peak at 2.39 Å in CR2 Tg is a feature of the surrounding aerogel. All spectra were measured using a 13 keV microfocus X-ray beam, except for #187 Tg1 which was measured at 11 keV.

Table 2. XRD measured d -spacings for indices hkl , with calculated unit cell dimensions.

	Unit Cell Dimension (Å)	220	311	222	400	422	511	440
CR2 Tg	8.353 (3)	2.952	2.518	2.411	2.09	1.705	1.607	1.477
#187 Tg1	8.355 (21)	2.954	2.516	2.405	2.089			
#178 Tg2	8.357 (10)		2.522	2.416	2.09		1.607	1.475
#178 Tg1a	8.370 (6)	2.959	2.526	2.413	2.093	1.71	1.61	1.479
Magnetite ^a	8.387 (1)	2.965	2.529	2.421	2.096	1.712	1.614	1.482
Magnetite ^b	8.396	2.968	2.531	2.424	2.099	1.714	1.616	1.484
Magnetite ^c	8.397	2.969	2.532	2.424	2.099	1.714	1.616	1.484
Trevorite ^d	8.363	2.957	2.521	2.414	2.091	1.707	1.609	1.478
Trevorite ^e	8.347	2.951	2.517	2.41	2.087	1.704	1.606	1.476
Maghemite ^f	8.33	2.945	2.512	2.405	2.083	1.7	1.603	1.473

^aReference material.

^bWechsler et al. (1984).

^cHaavik et al. (2000).

^dO'Driscoll et al. (2014).

^eBlesa et al. (1993).

^fPecharroman et al. (1995).

Referenced from American Mineralogical Crystal Structure Database (Downs and Hall-Wallace 2003).

Unit cell dimension error values calculated from standard deviation.

captured in aerogel, it is necessary to adjust for biasing effects during capture which under Stardust-like conditions have been shown to shift the true Fo value to an apparent lower value by up to 20 molar units (Foster et al. 2013). Therefore, all the Fo estimates in Table 3 based on Raman studies should be considered as lower estimates. Measurements made using Raman spectroscopy did not show the magnetite in the terminal grains of track #178, nor Fe-oxides of any kind,

whereas Fe-K XAS and XRD positively identified magnetite. The smaller Tg1b olivine grain only separates the magnetite Tg1a grain by $\sim 10 \mu\text{m}$, thus it is unlikely that any compression or melting of the surrounding aerogel could be causing significant difficulties with Raman detection of the magnetite, and this has never been considered an issue as shown by the detection of $10 \mu\text{m}$ sized analogue magnetite and hematite samples shot into aerogel (Bridges et al. 2010).

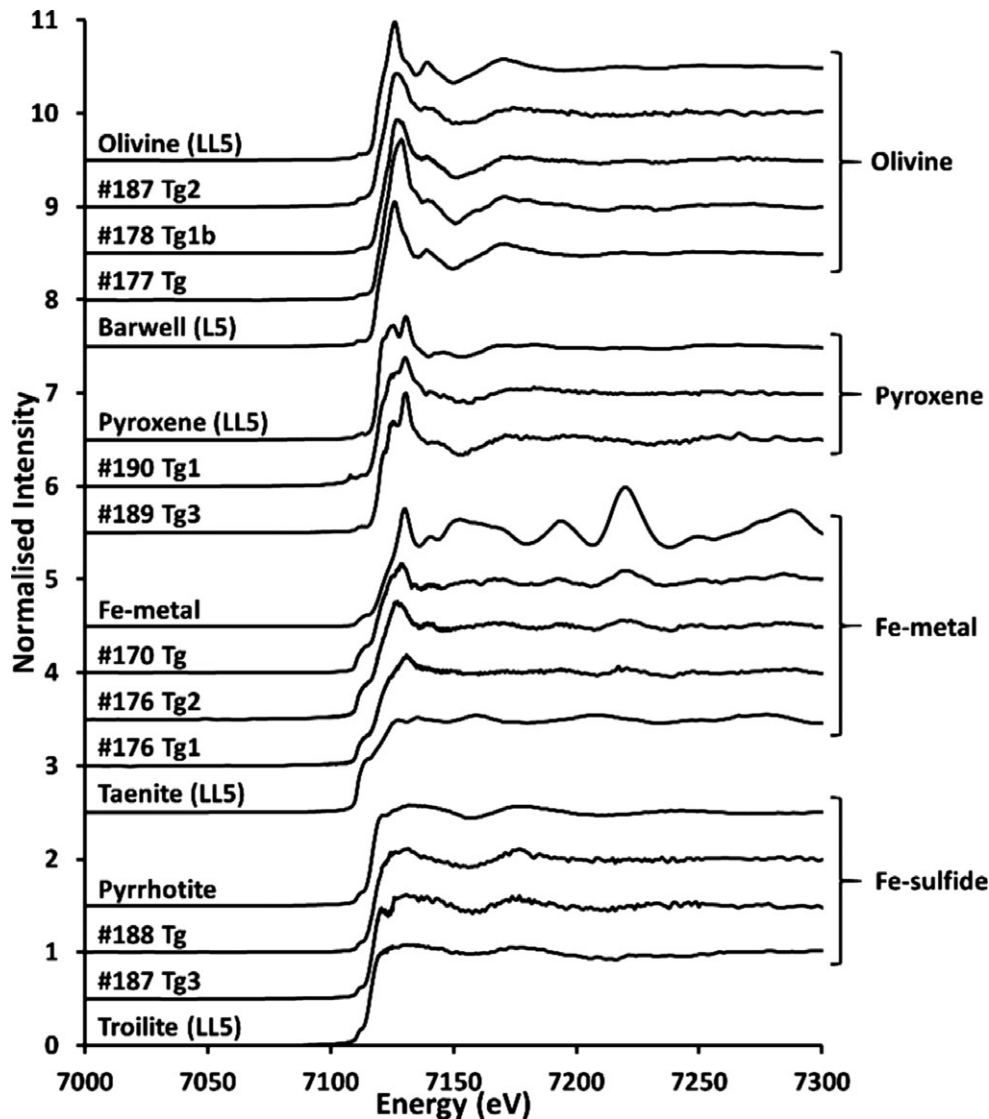


Fig. 6. The Fe-K XAS of other terminal grains in the Stardust keystone meteorites studied, including olivines, pyroxenes, Fe-metals, and Fe-sulfides, compared to standard reference materials and chondritic materials, Barwell (L5) and Tuxtuac (LL5).

The nondetection from Raman spectroscopy could be due to the surface state of the grain, as Raman measures the surface, thus if the surface of a grain has been modified during high-speed impact into the aerogel then the underlying core magnetite mineralogy may be obscured. Additionally, significant carbonaceous content was observed by Raman concentrated around the subgrain bulb region of Track #178, implying an organic-rich particle embedded with magnetite, perhaps even holding the original aggregate together like “glue” (Price et al. 2014).

Track C2065,4,187,0,0 (#187)

Figure 1b shows an optical microscope image of the type B track of #187, with a length of 590 μm , featuring

at least three terminal grains and a significant quantity of subgrain material in the bulbous region away from the track entrance. Each of the terminal grains measure approximately 5 μm in size, all consisting of a Fe-rich composition with some Ni present in Tg1 (Fig. 2).

The Fe-K XAS spectra of Fig. 4, with $1s \rightarrow 3d$ pre-edge centroid and Fe-K absorption edge positions of 7113.5 eV and 7121.0 eV, respectively, identify terminal grain Tg1 in track #187 as magnetite. Despite the weak spectra, the intense white-line and broad peaks in the EXAFS are also similar to the magnetite reference material and the magnetite terminal grain, Tg1a of track #178. Much like the magnetite terminal grains of track #178, the #187 Tg1 magnetite terminal grain may have a slightly higher oxidation state than that of the

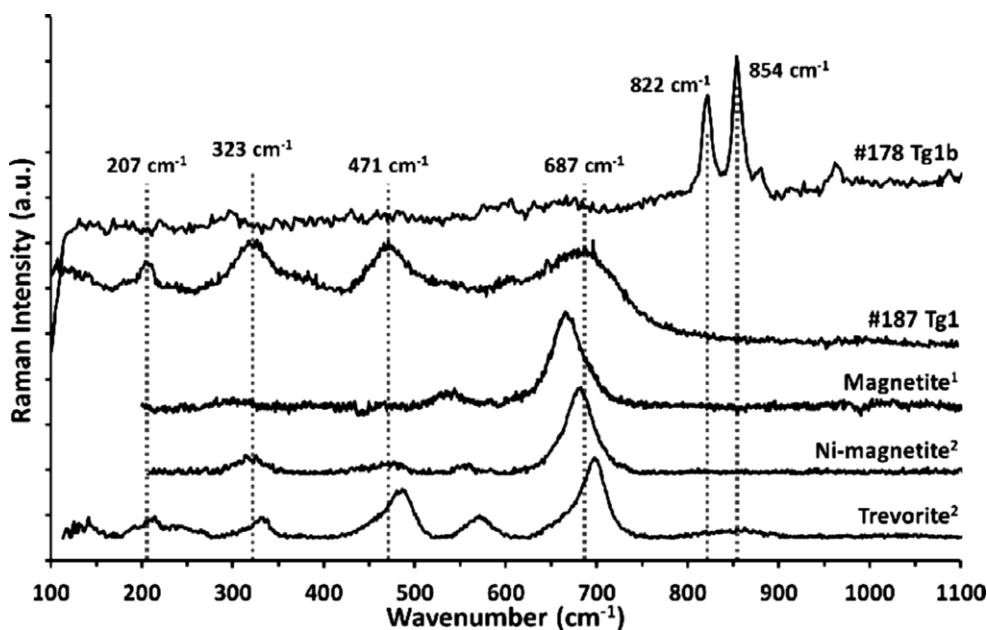


Fig. 7. Raman spectra of terminal grain Tg1b in track #178 and terminal grain Tg1 in track #187, measured using laser wavelengths of 473 nm and 633 nm, respectively. The positions of the two peaks at 821.7 cm^{-1} and 853.8 cm^{-1} , in #178 Tg1b, are used to estimate a forsterite (Fo_{80}) composition. ¹The magnetite spectra is of a standard reference material measured at the University of Kent (Bridges et al. 2010), using similar conditions as used for the Wild 2 terminal grains, with a laser wavelength of 633 nm. ²Reference spectra from the online RRUFF Project sample database (Lafuante et al. 2015) include Ni-bearing magnetite (RRUFF ID: R061111) and trevorite (RRUFF ID: R146860), measured with lasers at wavelengths of 785 nm and 780 nm, respectively. The peaks in the #187 Tg1 spectra are weak and broad, but the fingerprint of four Raman peaks are a close match for the Ni-bearing magnetite.

magnetite standard as shown by the positive shift in the Fe-K absorption edge position.

The transmission XRD (Fig. 5; Table 2), also positively identifies the Tg1 terminal grain of track #187 as magnetite with similar d -spacings and peak intensities at 2.954 Å, 2.516 Å, 2.405 Å, and 2.089 Å. Similar to the magnetite terminal grains of track #178, the estimated unit cell dimension of 8.355 Å is closer to trevorite and maghemite, consistent with traces of Ni, or alternatively, possible slight oxidation of the magnetite grain surface.

The Raman spectra for the #187 Tg1 terminal grain (Fig. 7) show a peak structure revealing bands at 207, 323, 471, and 687 cm^{-1} . The fingerprint Raman peaks somewhat resemble the Raman spectra of our magnetite standard reference material, despite the peaks for the #187 Tg1 terminal grain apparently shifted to higher wave numbers by $\sim 30\text{ cm}^{-1}$. A maghemite Raman spectra referenced in Hanesch (2009) presents bands at 350 and 512 cm^{-1} and a more prominent peak revealing two bands at 665 and 730 cm^{-1} , apparently displaced to higher wave numbers than the #187 Tg1 terminal grain. Comparing the fingerprint Raman peaks to reference spectra available from the online RRUFF Project sample database (Lafuante et al. 2015), Fig. 7 shows similarities between the #187 Tg1 terminal grain and the

fingerprint Raman wave numbers of different minerals of the magnetite series. Trevorite is displaced by $\sim 10\text{ cm}^{-1}$, to higher wave numbers but #187 Tg1 is a very close match to a Ni-bearing magnetite ($(\text{Fe}_{0.51}^{2+}\text{Ni}_{0.48}\text{Co}_{0.01})_{\Sigma=1}\text{Fe}_2^{3+}\text{O}_4$). Additionally, such a change in the position of the fingerprint Raman peaks may be explained by the temperature and shock history of the sample (Hibbert et al. 2014, 2015), in particular, the effects of aerogel impact during collection of the Wild 2 material.

The other terminal grains of track #187 were also measured for Fe-K XAS and XRD. Terminal grain Tg2 was found to have a Fe-K XAS spectra similar to olivine in the Tuxtuac (LL5) and Barwell (L5) ordinary chondrites (Fig. 6), with similar $1s \rightarrow 3d$ pre-edge centroid and Fe-K absorption edge positions at approximately 7112.3 eV and 7119.2 eV, respectively. The Fe-rich terminal grain Tg3, also with a minor Ni content, has a Fe-K XAS spectrum similar to Fe-sulfide, as shown in Fig. 6 with reference materials of troilite in the Tuxtuac (LL5) meteorite and a pyrrhotite standard.

Other Keystones Investigated

Track #170 is a type A track, measuring 3.2 mm in length with a $\sim 20\text{ }\mu\text{m}$ Fe-metal terminal grain (Fig. 1c),

Table 3. Composition of cometary samples based on microRaman spectroscopy.

Track	Grain	Composition
#170	Tg1	Mg-rich olivine endmember forsterite (Fo ₉₅)
#176	Tg1	Carbon (weak), enstatite, aerogel
	Tg2	Enstatite, aerogel (weak)
	Sg 'a'	Olivine (>Fo ₅₀), carbon (strong)
	Sg 'b'	Olivine (>Fo ₆₀), enstatite, aerogel
	Sg 'c'	Aerogel, unknown line at 227 cm ⁻¹
	Sg 'd'	Carbon (weak), aerogel
	Sg 'e'	Carbon, enstatite, (strong) aerogel
	Sg 'f'	Carbon, aerogel
	Sg 'g'	Carbon (strong), aerogel, unknown at 2325 cm ⁻¹)
	Sg 'h'	Carbon, aerogel
#177	Tg1 'a'	Olivine (>Fo ₈₀), carbon, aerogel
	Tg1 'b'	Olivine (>Fo ₈₀)
	Tg1 'c'	Carbon, enstatite
	Sg 'a'	Olivine (>Fo ₈₀)
	Sg 'b'	Olivine (>Fo ₈₅)
	Sg 'c'	Aerogel
	Sg 'd'	Aerogel
	Sg 'e'	Carbon (v. strong)
	Sg 'f'	Olivine (>Fo ₆₀), carbon
	Sg 'g'	Olivine (>Fo ₈₀), carbon
	Sg 'h'	Olivine (>Fo ₈₀), carbon (strong)
	Sg 'i'	Olivine (>Fo ₈₀), carbon (strong)
#178	Tg1a	Unknown (weak) lines at ~250 cm ⁻¹
	Tg1b	Olivine (>Fo ₈₀), carbon, aerogel
	Tg2	Unknown lines at 214.8 and 279.1 cm ⁻¹ , possibly metal oxide
	Sg 'a'	No definite lines (grain moved)
	Sg 'b'	Olivine (>Fo ₈₀), carbon (strong), aerogel
	Sg 'c'	Carbon, aerogel
	Sg 'd'	No definite lines
	Sg 'e'	Carbon
	Sg 'f'	Carbon
	Sg 'g'	Carbon (strong)
	Sg 'h'	Carbon (strong)
	Sg 'i'	Carbon (weak)
#187	Tg1	Possible magnetite spectrum
	Tg2	Very weak carbon
	Sg 'a'	No detectable Raman signal with 473 nm laser
	Sg 'b'	No detectable Raman signal with 473 nm laser
	Sg 'c'	No detectable Raman signal with 473 nm laser
	Sg 'd'	No detectable Raman signal with 473 nm laser
	Sg 'e'	No detectable Raman signal with 473 nm laser
	Sg 'f'	No detectable Raman signal with 473 nm laser
	Sg 'g'	No detectable Raman signal with 473 nm laser

Table 3. *Continued.* Composition of cometary samples based on microRaman spectroscopy.

Track	Grain	Composition
#188	Tg1	No detectable Raman signal
	Sg 'a'	Weak line at 1200 cm ⁻¹
	Sg 'b'	Weak carbon bands
	Sg 'c'	Weak carbon bands
#189	Tg1	Very weak hint of carbon with 532 nm laser
	Tg2	Weak hint of carbon with 633 nm laser
	Tg3	No detectable signal with any laser
#190	Tg1	No detectable signal
	Sg 'a'	Aerogel C-H lines
	Sg 'b'	Weak carbon

The Fo content of olivines should be considered a lower limit (Foster et al. 2013).

plus some Fe-rich residue subgrain material near the entrance of the track. This terminal grain was identified from XRF mapping with Fe and minor Cr detected (Fig. 2). The Fe-K XAS spectrum shows similarities to an Fe-metal foil reference material (Fig. 6), in particular the lack of a significant white-line peak suggests no unoccupied d-states for Fe-ions as found in pure Fe-metal. A negative shift of 3.5 eV in the Fe-metal terminal grain compared to reference Fe-metal foil (see Table 1) may be accounted for by a more intense $1s \rightarrow 3d$ pre-edge peak, which is also consistent with partial oxidation of the Fe-metal grain surface. The Fe-K EXAFS analysis also revealed a close fit to Fe-metal foil as expected with similar Fe-Fe bond lengths of ~2.48 Å, ~2.90 Å, ~3.63 Å, and ~4.80 Å.

The Fe-rich terminal grain of track #170 also contains some Cr, as shown in the #170 Tg XRF spectrum (Fig. 2), and thus was measured for Cr-K XAS. Analyses of the Cr-EXAFS revealed a first shell Cr-O bond length of 2.04 Å, and a Cr-O-Si bond length of 2.79 Å, revealing the grain to be a Cr-bearing silicate. This is in contrast to the chromite reference material measured, where Cr-EXAFS analyses revealed, as expected, Cr-O and Cr-Cr bond lengths of 1.99 Å and 2.98 Å, respectively. Raman spectra analysis of this Cr-bearing silicate found a best fit to the Mg-rich olivine endmember forsterite (Table 3), with two peaks at 824 and 856 cm⁻¹, whereas the pure Fe-metal in the grain would not have exhibited Raman scattering (Price et al. 2012).

The Fe-K XAS spectrum shows that the iron in #170 Tg was dominantly metallic. For a chondritic Fe-metal grain, a minor content of Ni would also be expected, but the XRF spectrum (Fig. 2) shows no apparent evidence of any Ni content, and nor does the Fe-K XAS spectrum (Fig. 6) show any similarities

between #170 Tg and a LL5 chondrite taenite (Fe,Ni-metal) grain. If Ni is present in #170 Tg, the quantity is certainly below the detection limits of the XRF spectrum, and such a minor Ni content would reveal very little variation in the Fe-K XAS structure of a dominantly Fe-metal phase, compared to the Fe-K XAS structure for the LL5 chondrite taenite, which has a Ni composition of 38 wt% (Graham et al. 1988).

Similarly, XRF of the 4 μm terminal grain in the 1.35 mm long #177 track (Fig. 1d) shows a minor presence of Cr in a Fe-rich grain, with a first shell Cr-O bond length of 2.03 Å, and a Cr-O-Si bond length of 2.78 Å revealed in the Cr-K EXAFS analysis. However, unlike the terminal grain of #170, which was predominantly Fe-metal, the olivine identity was revealed in the Fe-K XAS (Fig. 6), with $1s \rightarrow 3d$ pre-edge centroid and Fe-K absorption edge positions at 7112.5 eV and 7119.6 eV, respectively, again with a minor ferric (and Cr) content in the olivine. Raman analysis also found this olivine grain to be Mg-rich forsterite ($>F_{080}$), plus the detection of some carbon (Table 3).

Track #176 is a type B track with two styli measuring 380 μm in length (Fig. 1e). Both terminal grains measured $\sim 5 \mu\text{m}$ and are Fe rich, with Tg2 positively identified as Fe-metal from the Fe-K XAS analysis (Fig. 6), plus a significant presence of C identified by Raman analysis. Tg1 remains unidentified due to weak structural features presented in the Fe-K XAS spectra, but certain features such as a large broad $1s \rightarrow 3d$ pre-edge peak at 7112.9 eV and a possible peak feature at ~ 7220 eV in the EXAFS (see Fig. 6) suggest similarities to Fe-metal, and XRF showed the grain also has a minor Ni content. The Fe-metal in #176 was not detected by the Raman analyses, as expected due to the lack of scattering from metal, but enstatite was detected by Raman, which may have been masked by the presence of Fe-metal in the Fe-K XAS measurements.

The Fe-K XAS spectra for the $\sim 5 \mu\text{m}$ terminal grain, at the end of the 460 μm long type B #188 track (Fig. 1f), showed similarities to the spectra for the Tg3 Fe,Ni-sulfide in the track #187, as well as the Fe-sulfide reference materials, including $1s \rightarrow 3d$ pre-edge centroids at ~ 7111.8 eV and the lack of a prominent white-line peak in the XANES (Fig. 6).

Tracks #189 and #190, measuring 740 μm and 810 μm in length, respectively, are both type B tracks present in the same Stardust aerogel keystone (Fig. 1g). The $\sim 7 \mu\text{m}$ terminal grain, Tg1, of track #189 was found to have variable amounts of Fe and Ca, but the grain remained undetected by Raman except for a hint of carbon (Table 3). Fe-K XAS measurements of the #189 Tg1 terminal grain revealed a similar spectral

structure to magnetite (Fig. 4), including closely matching $1s \rightarrow 3d$ pre-edge centroid and Fe-K absorption edge positions at 7113.1 eV and 7121.1 eV, respectively, although the intensity of the $1s \rightarrow 3d$ pre-edge peak is significantly reduced compared to reference and other cometary magnetites shown in Fig. 4 (inset). XRD analysis of the #189 Tg1 terminal particle was not successful.

The $\sim 5 \mu\text{m}$ Tg3 terminal grain of #189 and $\sim 7 \mu\text{m}$ terminal grain of #190 both have a Fe-rich composition, with minor Cr and Mn. Raman was unable to detect anything, except for some weak hints of carbon. However, from the Fe-K XAS measurements (although the spectral intensity was not strong in #190, hence no $1s \rightarrow 3d$ pre-edge centroid reported in Table 1), these two grains do have Fe-K EXAFS structure, along with the latter parts of the Fe-K XANES, revealing similarities to pyroxene minerals we measured in the Tuxtuac (LL5) ordinary chondrite (Fig. 6).

Carbonaceous Chondrite Analogue Sample

The SEM analysis of the NWA 10256 CR2 chondrite thin section revealed 58% of the meteorite to be composed of chondrules. Many of the chondrules measured >1 mm in diameter, composed of pyroxenes ($\text{En}_{27-99}\text{Wo}_{0-6}\text{Fs}_{1-67}$) and olivines (Fo_{66-99}). Surrounding the chondrules is a matrix of Fe-rich olivines (Fo_{41-81}), Fe-sulfides, Fe,Ni-metals, and Fe-oxides.

The XRF analysis of the CR2 terminal grain (Fig. 2) reveals an Fe-rich content, with a trace amount of Ni, much like the composition of the magnetite terminal grains of Stardust tracks #178 (Tg1a and Tg2) and #187 (Tg1). This grain has been identified as magnetite from the XRD and Fe-K XAS, measuring a $1s \rightarrow 3d$ pre-edge centroid position at 7113.1 eV, all similar to the reference magnetite powder and the Stardust magnetite terminal grains (see Table 1). Like the Stardust magnetite grains, there is an increased shift in the energy for the Fe-K absorption edge positions, suggesting increased oxidation, over pure magnetite.

The XRD analysis of the CR2 grain gave d -spacings and derived unit cell dimensions similar to magnetite, as shown in Fig. 5 and Table 2, but also like the Stardust terminal grains there is a minor discrepancy between the unit cell dimension of the CR2 magnetite (at 8.353 Å) and the pure magnetite (8.387 Å), where the CR2 magnetite has unit cell dimensions closer to that of the trevorite (8.363 Å) and/or maghemite (8.33 Å) samples referenced in Table 2.

For comparison, a magnetite measured from the polished thin section of the NWA 10256 CR2 meteorite revealed a Fe-rich content in the XRF with a minor Cr

content, rather than a Ni content like in the terminal grain (see Fig. 2). The Fe-K XAS analysis estimated a $1s \rightarrow 3d$ pre-edge centroid and absorption edge position at 7113.0 eV and 7119.4 eV, but the absorption edge in particular is not a close match for the light-gas gunshot magnetite grain or the Stardust magnetite grains. Instead the thin section material more closely resembles a thick ($>30 \mu\text{m}$) concentrated magnetite standard (also shown in Fig. 4) which has resulted in a shift in the absorption edge energy position and a less prominent white-line peak and EXAFS, due to self-absorption in the beam.

The ESEM-EDX analysis of the NWA 10256 thin section also revealed the presence of magnetite grains with some Cr content ($<1\%$ Cr). Magnetite was found to be less than 1% of the sample, mostly found within $\sim 300 \mu\text{m}$ wide features consisting of Fe, Ni-metals and sulfides. Ni-bearing magnetite similar to the CR2 magnetite terminal grain was also identified in the CR2 thin section, during analysis using an ESEM.

DISCUSSION

Wild 2 Links to Carbonaceous Chondrite

Before the Stardust mission, comet formation had been considered the result of pre-solar ice condensing on interstellar dust aggregates (Greenberg 1982). However, investigating the cometary particles returned by Stardust has revealed the mineral assemblage not of an interstellar ice-dust aggregate formation with little chemical modification, but largely consisting of high-temperature forming minerals, and a lack of interstellar grains. This includes ferromagnesian silicates, such as olivines and low-Ca pyroxenes, along with many Fe,Ni-sulfides and Fe,Ni-metals, with at least 50% of that material in crystalline form (Zolensky et al. 2006; Westphal et al. 2009). The observed lack of interstellar grains may, however, be an artifact of the capture process; it has been reported by Floss et al. (2013) that once such a collection bias is corrected for, the Stardust results are compatible with interstellar grain abundances in primitive IDPs.

The results of some of the Wild 2 samples in this investigation are consistent with those of earlier reports, including ferromagnesian silicates of olivine in tracks #178 and #187, with a Cr-rich olivine in #177, plus a Cr-silicate in track #170, and pyroxenes in tracks #189 and #190. Fe,Ni-sulfides were also identified in the terminal grains of tracks #187 and #188, and Fe-metals in #170 and #176.

Such a mineral assemblage of ferromagnesian silicates, metals, and sulfides, and other discoveries of

CAIs and chondrule-like fragments reveal the many mineralogical affinities with carbonaceous chondrites for the collected Wild 2 material, more so than interplanetary dust particles (IDPs) (Brearley and Jones 1998; Hutchison 2004). Additional links to carbonaceous chondrites include reported chondrules and CAIs. Investigated cometary particles have revealed oxygen isotopic composition similar to asteroidal chondrules (Nakamura et al. 2008; Bridges et al. 2012), and Al-rich diopside, pigeonite, and minor forsterite and enstatite are consistent with Al-rich chondrules (Bridges et al. 2012). The Iris particle from Stardust track #74 is similar to late-forming chondrules in CR chondrites (Ogliore et al. 2012). The Inti particle from track #25 (Simon et al. 2008) and another, Coki, from #141 (Matzel et al. 2010) also contained Al-rich, Ti-bearing, clinopyroxenes, with Mg-Al spinel and anorthite. Inti also featured perovskite, Fe,Ni-metal and osbornite grains, and melilite, consistent with CAIs (Simon et al. 2008). Simon et al. (2008) found the Inti particle to be similar to major phases in most CAIs found in CV3, CH, CO, and CM2 chondrites, forming at high temperatures of $>1400 \text{ K}$. The presence of CAIs and chondrules would exclude CI chondrite meteorites which have a very low modal abundance of such constituents, if any at all (Hezel et al. 2008). However, it is notable that not all of the Wild 2 affinities point directly toward carbonaceous chondrites. Many of the pyroxenes in type B tracks are rich in Na and Cr. These assemblages have been named “Kool” (Kosmochloric high-Ca pyroxene and FeO-rich olivine) grains and are similar to many IDPs (Joswiak et al. 2009). Ishii et al. (2008) and Westphal et al. (2009) concluded that the Wild 2 cometary materials resemble chondritic meteorites of the asteroid belt, and were less similar to IDPs, but suggested that they could not be recognized as any specific chondrite type.

Magnetite in Wild 2

Magnetite mineral grains firmly identified in the terminal particles of Stardust tracks, including the three magnetite grains identified in tracks #178 and #187 in this investigation, provide further evidence for the mineralogical affinities of Wild 2 to carbonaceous chondrites. Magnetite is rare in previously investigated Stardust samples, but it has been identified as subgrain in #134 (Changela et al. 2012). A minor amount of magnetite was also found in the subgrain of #80 (Stodolna et al. 2012a). A terminal grain of Cr-rich magnetite was reported in track #183 by De Gregorio et al. (2015), part of an assemblage of poorly graphitized carbon (PGC) and cohenite. Those authors addressed the $\delta^{13}\text{C}$ and $\delta^{15}\text{N}$ isotopic analyses of the

PGC particles suggesting a nebular origin, rather than a cometary parent body formation.

The Fe-oxide particles in some tracks, such as in the 100–200 nm subgrain residue material of tracks #41 and #121, may have become oxidized by capture heating in the aerogel, thus resulting in ferric material such as hematite or goethite from what may have originally been magnetite (Bridges et al. 2010). Subgrain material identified as hematite was observed near the entrance to track #170. Also, potential oxidation of magnetite grains is evident in the Stardust magnetite of tracks #178 and #187, where an increased shift in the Fe-K absorption edge position suggests a higher Fe³⁺ content, over that of pure Fe₃O₄ magnetite, while the 1s → 3d pre-edge and EXAFS structure remained consistent for magnetite. A similar discrepancy was observed between the aerogel shot CR2 magnetite and the Fe₃O₄ powdered magnetite standard sample. It is uncertain whether this shift in the Fe-K absorption edge, where there is no discrepancy in the 1s → 3d pre-edge centroid, could in fact be an effect of the impact with aerogel, such as the heated oxidation during capture suggested by Bridges et al. (2010), or the ferric content of the grain itself causing the shift in the XAS energy. The grains investigated are comparatively large (<6 μm), so heating from the aerogel impact would only result in amorphous rims <1 μm deep, with the cores of the grains remaining unaltered (Noguchi et al. 2007; Stodolna et al. 2012b).

Additionally, the XRD results are consistent with crystalline magnetite, but there were small discrepancies in the estimated unit cell dimensions, for both Stardust magnetite and the aerogel shot CR2 magnetite. This could be explained by surface oxidation, reducing the cell dimensions to that of maghemite. However, the samples of this investigation more closely resemble the unit cell dimensions of trevorite (Ni²⁺Fe₂³⁺O₄). Trevorite is a mineral from the magnetite series, but there is only a trace of Ni evident in each of the Stardust magnetite samples. Thus, Ni has only partially replaced the Fe²⁺ in the magnetite, resulting in minor Ni-bearing magnetite (trevorite-magnetite solid solution). Fe,Ni-metal is present in the NWA 10256 CR2 sample, and Fe,Ni-metal has been identified in Stardust samples, including a terminal grain in track #176 and magnetite residue present along with Fe,Ni-metals in track #41 (Bridges et al. 2010).

Magnetite Formation

Terrestrially, Ti-magnetites are one of the last high-temperature minerals to crystallize in the interstices of many igneous rocks, particularly in the more basic basalt rock types (Bateman 1951). Similarly,

titanomagnetite grains also feature in the groundmass of basaltic achondrite meteorites such as angrites (Middlefehldt et al. 1998) and the Martian meteorites (McSween and Treiman 1998). Equilibrated chondrites also contain Ti-magnetite and ilmenite crystallizing with increased metamorphism (Chaumard et al. 2009).

However, compared to high-temperature-forming Ti-magnetites, far more abundant in carbonaceous chondrites are Ti-free magnetites. In particular, Ti-free magnetite is the second most abundant phase in CI chondrites (Choi et al. 1997; Krot et al. 2000). These Ti-free magnetite phases in carbonaceous chondrites are associated with oxidation and aqueous alteration (Brearley and Jones 1998; Hutchison 2004; Weisberg et al. 2006), which is typical also of terrestrial Ti-free magnetites resulting from oxidation and/or hydrous reaction with ferromagnesian silicates (Haggerty and Baker 1967; Sanderson 1974). Along with magnetite, other alteration phases can also be found throughout the carbonaceous chondrites, such as Fe-Mg serpentines and saponite smectites in CI, CR, and CV chondrites, as well as sulfates and carbonates (Brearley 2006).

Other Fe-oxides such as hematite are more rare but present in carbonaceous chondrites, for example, CM2 and CI meteorites (Uesugi et al. 2013), as well as in the LL3 chondrite Krymka (McSween and Taylor 1978; Semenenko et al. 2005). Magnetite is also typically found in chondrites as a terrestrial weathering product along with other Fe³⁺-rich crystalline and amorphous products (King and King 1981; Gooding 1981, 1986; Popp et al. 2002). Additionally, maghemite (γ-Fe₂O₃) has also been found in unequilibrated chondrites such as the LL3 Semarkona meteorite, but is rare (Hutchison et al. 1987; Alexander et al. 1989; Keller 1998). Trevorite in chondrites is also rare, but was identified in the Renazzo CR2 meteorite, based on the XRD determined unit cell dimensions of 8.44 Å (Mason and Wiik 1962). Ni-rich magnetite is also present in the Bencubbin CBA meteorite (Barber and Hutchison 1991), and in general is more common in extraterrestrial spinel than terrestrially formed spinel (Yu-Qui et al. 1997).

The CR3 carbonaceous chondrites contain no magnetites, but CR2 chondrites are the most aqueously altered members of the CR group. For instance, the chondrule mesostases have been hydrated to form phyllosilicate rims around the chondrules, as well as magnetites that have replaced metallic Fe,Ni-metal (Harju et al. 2014). Le Guillou et al. (2015) suggested that a progressive alteration is evident in a series of CR meteorites categorized from type CR3 to CR2, where amorphous Fe²⁺-silicate particles in CR matrices that formed after accretion were hydrated and oxidized, resulting in the presence of coarse-grained crystalline Mg-saponite and fine-grained serpentine solid solutions.

During this oxidation, Fe^{3+} was redistributed from the silicates to form magnetite and hematite grains.

Without a definite context for the mineralogical setting for the Stardust grains, other formation processes for Ti-free magnetite in planetary materials cannot be definitively excluded. Recent investigations of CV3 chondrites Vigarano and Kaba by Marrocchi et al. (2016) have discovered Ti-free magnetite in chondrules formed under impact-generated high-temperature magmatic conditions. The sulfide-associated magnetites are surrounded by a glassy chondrule mesostasis that has remained unaltered, demonstrating that the magnetite formation did not occur via aqueous alteration processes. It has also been proposed that CV3 magnetite formation occurred in the solar nebula. Hong and Fegley (1998) demonstrated experimentally (using the Gibeon iron meteorite) the oxidation of Fe-metal samples into magnetite via the net reaction $3\text{Fe (metal)} + 4\text{H}_2\text{O (gas)} = \text{Fe}_3\text{O}_4 \text{ (magnetite)} + 4\text{H}_2 \text{ (gas)}$, where magnetite formed at temperatures of 91–442 °C and at 1 bar atmospheric pressure in variable gas mixtures of H_2 , H_2O , and He. The Bulk Gibeon sample had an average atomic composition of $\text{Fe}_{91.5}\text{Ni}_{8.1}\text{Co}_{0.4}$, and the minor Ni alloy also oxidized along with the magnetite to produce NiFe_2O_4 (trevorite), rather than leaving small Ni-metal remnants, and experimentally had very little variation (<1 °C) in the temperature required to form magnetite. However, in a study of such processes, Krot et al. (1995) suggested an asteroidal parent body formation to be likely for CV3 magnetites, calculating temperatures of <300 °C for the formation of alteration minerals, including magnetite veins that cross-cut the chondrule rims, indicating a formation after accretion of the asteroid (Krot et al. 1995, 1998a, 1998b).

Aqueous alteration mineral assemblages, rich in magnetite are especially prominent in the CI and CM chondrites, with a 2–9 vol% in CI chondrites, ranging 10–30 μm in grain size (Bland et al. 2004; King et al. 2015; Brearley and Jones 1998), and 0.6–5.2 vol% in CM2 chondrites, with grain sizes ranging 0.25–20 μm in diameter (Howard et al. 2011a; Brearley and Jones 1998). Other measured chondrite magnetite contents include 0.2 vol% in CV3 chondrites (Bland et al. 2004), and 1–2 vol% in CR chondrites (Howard et al. 2011b). It is apparent across the various chondrite class and types that with an increased magnetite content there is complementary evidence in the mineral assemblages of increased hydration (Howard et al. 2011a). Therefore, there is conclusive strong evidence that in oxidized chondrites, the magnetite and hydrous mineral phases occur predominantly as a result of hydrothermal fluid–rock interaction upon metals and FeMg silicates within postaccretion asteroid parent-bodies. Water ice would have accreted along with the primitive material, and

^{26}Al -induced radiogenic melting of the water ice could have initiated hydrothermal fluid flow within the asteroid during the first few million years of its history (Miyamoto et al. 1981; Ghosh and McSween 1998; Merk et al. 2002).

However, the lack of mineralogical context provided by the Stardust collection prohibits absolute proof of a Wild 2 parent body aqueous alteration for the magnetite. It is important to note that the magnetites in aqueously altered chondrites are typically embedded in a fine-grained matrix of phyllosilicates, as they are another remnant of hydrothermal alteration of the ferromagnesian silicates (Brearley and Jones 1998; Brown et al. 2000; Fujiya et al. 2013). Out of over 200 tracks and many Al-foil impacts investigated there is a noticeable absence of phyllosilicates (Westphal et al. 2017), despite the many links to carbonaceous chondrites. This absence of phyllosilicates may be due to such friable material not remaining intact during aerogel capture (Wozniakiewicz et al. 2015), or it could be an intrinsic feature of Wild 2 that there are no phyllosilicates. We also note that there is a relatively low abundance (~1%) of magnetite in NWA 10256. Identifying this phase alone in a single keystone track, for this aerogel shot CR2 sample, suggests that there may be a previously unrecognized selection effect during capture related to the densities and friable nature of minerals in the Wild 2 material. Experimental studies of hypervelocity impacts have shown that there is a correlation between the ratio of penetrator and target density with penetration depth. Dehn (1987) and Christiansen and Friesen (1997) both showed that the penetration depth was proportional to the square root of the ratio of projectile and target densities. For Stardust samples, the higher density minerals—such as magnetite (5150 kg m^{-3})—will tend to penetrate further. This can explain the preferential preservation of magnetite in the terminal grains. Likewise it may also explain the apparent absence of low-density minerals—notably phyllosilicate—in the tracks as its penetration depth may be much shorter. Noguchi et al. (2007) did demonstrate that, when shot into aerogel at $>6 \text{ km s}^{-1}$, powdered phyllosilicate grains of serpentine and cronstedtite remained intact during capture, although with some surficial melting. The resulting terminal grains measured 10–30 μm in diameter, were reduced to <20% of their original volume. Similar light-gas gun experiments firing phyllosilicates lizardite and cronstedtite into simulated Stardust Al-foil at 6 km s^{-1} , performed by Wozniakiewicz et al. (2015), resulted in material completely melting upon impact and a loss of volatiles but chemically the Si-ratio composition was mostly retained. In addition to magnetite, the alteration present in CR2 meteorites typically includes

phyllosilicates of saponite and Fe-Mg serpentine, along with Fe-sulfides and sometimes calcite carbonates (Brearley 2006). The CR2 affinities hinted at by magnetite in Wild 2 are not easily reconciled with the apparent absence of phyllosilicates in Stardust tracks. However, the experimental evidence available suggests that preservation of any cometary phyllosilicate may have been inhibited.

With thousands of cometary particles collected by Stardust, a more complete overview of the Comet Wild 2 constituents is still developing and ongoing, as more and more samples are extracted and analyzed. By refining the compositional quantities of the ferromagnesian silicates, and in particular chondrule-like fragments, along with oxides and metals, and the successful identification of phyllosilicate and more magnetites, the affinities to carbonaceous chondrites may eventually link Comet Wild 2 to specific meteorite classes or mixtures. As yet a dominant class signature remains elusive and it may be that Wild 2 has sampled a mixture of carbonaceous chondrite classes.

The carbonaceous chondrite affinities of the Wild 2 mineral assemblage including magnetite, may indicate that a large-scale exchange from the early inner solar nebula toward the 30 AU outer regions where icy bodies formed occurred. By this scenario a diffusive protoplanetary disk would also be responsible for the presence of other high-temperature-processed material found in the Wild 2 samples (Ciesla 2011). However, Hughes and Armitage (2010) found no model that would sustain radial drift for large particles (>mm), but smaller particles (<20 μm) drift to the outer solar system could be stabilized for at least a short period of time (<10⁶ yr). Therefore, for this diffusive transport it would be necessary for the asteroidal material, in which the magnetites reside, to have been pulverized to dust before diffusion outward to the cometary forming region and rapidly accreted. Alternatively, Nayakshin et al. (2011) proposed that the high-temperature-processed materials formed within massive giant planet embryos (GEs) in the very young outer protoplanetary disk, at distances of ~100 AU from the Sun, followed by a “tidal downsizing” that drew the terrestrial and gas giant planets to their current orbits along with many impacts that produced the material for cometary accretion.

CONCLUSIONS

The mineralogy of Comet Wild 2 terminal grains and subgrain material has been studied using Fe-K and Cr-K XAS and transmission XRD experiments and Raman analyses.

1. At least three magnetite terminal grains, ranging in size from ~6 to 10 μm , have been identified using XANES and transmission XRD analyses, in keystones C2045,4,178,0,0 (#178) and C2065,4,187,0,0 (#187). By analogy with carbonaceous chondrites, this Ti-free magnetite probably formed at low temperatures as a result of water-rock reactions, such as the hydrous alteration of coexisting ferromagnesian silicates and Fe,Ni-metal or sulfide, also found in the Wild 2 constituents.
2. CR2 homogenized powder was shot into aerogel at 6.1 km s⁻¹, simulating the Stardust encounter, and an aerogel keystone prepared similar to Stardust track keystones. This experiment was to test the consensus that Wild 2 has affinities to carbonaceous chondrites, and the results demonstrated the preservation of magnetite from CR2 powder—analogue to the Wild 2 coma—during impact into aerogel.
3. Other minerals identified in Comet Wild 2 samples, during this investigation, include terminal grains of high-temperature-forming materials, such as Fe-metal, Fe,Ni-metal, ferromagnesian olivine, and Cr-bearing silicates. The tracks also included Fe-rich and Fe,Ni-sulfide residue subgrain material. This adds to the findings of previously studied Stardust tracks, showing affinities between carbonaceous chondrites and the Comet Wild 2 material, including the juxtaposition of reduced and oxidized Fe-rich minerals.
4. Further investigation of powdered carbonaceous chondrite shot into aerogel at 6.1 km s⁻¹ may provide a more detailed analogue comparison for Comet Wild 2 and the effects that aerogel impact and mineral density or hardness can have on the preserved mineral assemblage.

Acknowledgments—We thank the NASA JSC Stardust Sample Curator for the loan of the Stardust aerogel track samples, prepared at the University of California at Berkeley and NASA-JSC. The Diamond Beamline I18 staff Fred Mosselmans and Konstantin Ignatyev are thanked for the help in data acquisition, during beamtimes sp1833-1 (Changela et al. 2012), sp7487-1 (December 2011), sp9418-1 (December 2013), sp10328-1 (December 2014), and sp13690-1 (July 2016). We also thank Graham Clark, Vinay Patel, and Lin Marvin of the University of Leicester for their support with SEM analysis of the meteorite samples. STFC is thanked for operation of the light-gas gun and Raman spectrometer (University of Kent). EXAFS research involved the use of DL_EXCURV v1.01 via the SPECTRE High Performance Computing Facility at the University of

Leicester. J. C. Bridges, M. J. Burchell, and M. C. Price acknowledge funding from STFC to support this work.

Editorial Handling—Dr. Michael Zolensky

REFERENCES

- Alexander C. M. O'D., Barber D. J., and Hutchison R. 1989. The microstructure of Semarkona and Bishunpur. *Geochimica et Cosmochimica Acta* 53:3045–3057.
- Barber D. J. and Hutchison R. 1991. The Bencubbin stony-iron meteorite breccia: Electron petrography, shock-history and affinities of a “carbonaceous chondrite” clast. *Meteoritics* 26:83–95.
- Basham M., Filik J., Wharmby M. T., Chang P. C. Y., El Kassaby B., Gerring M., Aishima J., Levik K., Pulford B. C. A., Sikharulidze I., Sneddon D., Webber M., Dhesi S. S., Maccherozzi F., Svensson O., Brockhauser S., Náray G., and Ashton A. W. 2015. Data Analysis Workbench (DAWN). *Journal of Synchrotron Radiation* 22:853–858.
- Bateman A. M. 1951. The formation of late magmatic oxide ores. *Economic Geology* 46:404–426.
- Berger E. L., Zega T. J., Keller L. P., and Lauretta D. S. 2011. Evidence for aqueous activity on comet 81P/Wild 2 from sulfide mineral assemblages in Stardust samples and CI chondrites. *Geochimica et Cosmochimica Acta* 75:3501–3513.
- Berry A. J., O'Neill H. S. C., Jayasuriya K. D., Campbell S. J., and Foran G. J. 2003. XANES calibrations for the oxidation state of iron in silicate glass. *American Mineralogist* 88:967–977.
- Bland P. A., Cressey G., and Menzies O. N. 2004. Modal mineralogy of carbonaceous chondrites by X-ray diffraction and Mossbauer spectroscopy. *Meteoritics & Planetary Science* 39:3–16.
- Blesa M. C., Amador U., Moran E., Menendez N., Tornero J. D., and Rodriguez-Carvajal J. 1993. Synthesis and characterization of nickel and magnesium ferrites obtained from α -NaFeO₂. *Solid State Ionics* 63:429–436.
- Brearely A. J. 2006. The action of water. *Meteorites and the early solar system II*, edited by Laurette D. S. and McSween H. Y. Jr. Tucson, Arizona: The University of Arizona Press. pp. 584–624.
- Brearely A. J. and Jones R. H. 1998. Chondritic meteorites. *Planetary materials*, edited by Papike J. J., Reviews in Mineralogy, vol. 36. Washington, D.C.: Mineralogical Society of America. pp. 3.1–3.398.
- Bridges J. C., Burchell M. J., Changela H. G., Foster N. J., Creighton J. A., Carpenter J. D., Gurman S. J., Franchi I. A., and Busemann H. 2010. Iron oxides in comet 81P/Wild 2. *Meteoritics & Planetary Science* 45:55–72.
- Bridges J. C., Changela H. G., Nayakshin S., Starkey N. A., and Franchi I. A. 2012. Chondrule fragments from Comet Wild2: Evidence for high temperature processing in the outer solar system. *Earth and Planetary Science Letters* 341–344:186–194.
- Brown P. G., Hildebrand A. R., Zolensky M. E., Grady M., Clayton R. N., Mayeda T. K., Tagliaferri E., Spalding R., MacRae N. D., Hoffman E. L., Mittlefehldt D. W., Wacker J. F., Bird J. A., Campbell M. D., Carpenter R., Gingerich H., Glatiotis M., Greiner E., Mazur M. J., McCausland P. J. A., Plotkin H., and Mazur T. R. 2000. The fall, recovery, orbit, and composition of the Tagish Lake meteorite: A new type of carbonaceous chondrite. *Science* 290:320–325.
- Brownlee D., Tsou P., Aléon J., Alexander C. M. O. D., Araki T., Bajt S., Baratta G. A., Bastien R., Bland P., Bleuet P., Borg J., Bradley J. P., Brearley A., Brenker F., Brennan S., Bridges J. C., Browning N. D., Brucato J. R., Bullock E., Burchell M. J., Busemann H., Butterworth A., Chaussidon M., Chevront A., Chi M., Citala M. J., Clark B. C., Clemett S. J., Cody G., Colangeli L., Cooper G., Cordier P., Daghlian C., Dai Z., D'Hendecourt L., Djouadi Z., Dominguez G., Duxbury T., Dworkin J. P., Ebel D. S., Economou T. E., Fakra S., Fahey S. A. J., Fallon S., Ferrini G., Ferroir T., Fleckenstein H., Floss C., Flynn G., Franchi I. A., Fries M., Gainsforth Z., Gallien J.-P., Genge M., Gilles M. K., Gillet P., Gilmour J., Glavin D. P., Gounelle M., Grady M. M., Graham G. A., Grant P. G., Green S. F., Grossemy F., Grossman L., Grossman J. N., Guan Y., Hagiya K., Harvey R., Heck P., Herzog G. F., Hoppe P., Hörz F., Huth J., Hutcheon I. D., Ignatyev K., Ishii H., Ito M., Jacob D., Jacobsen C., Jacobsen S., Jones S., Khoswiak D., Jurewicz A., Kearsley A. T., Keller L. P., Khodja H., Killoyne A. L. D., Kissel J., Krot A., Langenhorst F., Lanzirrotti A., Le L., Leshin L. A., Leitner J., Lemelle L., Leroux H., Liu M.-C., Luening K., Lyon I., MacPherson G., Marcus M. A., Marhas K., Marty B., Matrajt G., McKeegan K., Meibom A., Mennella V., Messenger K., Messenger S., Mikouchi T., Mostefaoui S., Nakamura T., Nakano T., Newville M., Nittler L. R., Ohnishi I., Ohsumi K., Okudaira K., Papanastassiou D. A., Palma R., Palumbo M. E., Pepin R. O., Perkins D., Perronnet M., Pianetta P., Rao W., Rietmeijer F. J. M., Robert F., Rost D., Rotundi A., Ryan R., Sandford S. A., Schwandt C. S., See T. H., Schlutter D., Sheffield-Parker J., Simionovici A., Simon S., Sitnitsky I., Snead C. J., Spencer M. K., Stadermann F. J., Steele A., Stephan T., Stroud R., Susini J., Sutton S. R., Suzuki Y., Taheri M., Taylor S., Teslich N., Tomeoka K., Tomioka N., Toppani A., Trigo-Rodríguez J. M., Troadec D., Tsuchiyama A., Tuzzolino A. J., Tylliszczak T., Uesugi K., Velbel M., Vellenga J., Vicenzi E., Vincze L., Warren J., Weber I., Weisberg M., Westphal A. J., Wirick S., Wooden D., Wopenka B., Wozniakiewicz P., Wright I., Yabuta H., Yano H., Young E. D., Zare R. N., Zega T., Ziegler K., Zimmerman L., Zinner E., and Zolensky M. 2006. Comet 81P/Wild 2 under a microscope. *Science* 314:1711–1716.
- Bunker G. 2010. *Introduction to XAFS: A practical guide to X-ray absorption fine structure spectroscopy*. New York: Cambridge University Press.
- Burchell M. J., Cole M. J., McDonnell J. A. M., and Zarnecki J. C. 1999. Hypervelocity impact studies using the 2 MV Van de Graaff accelerator and two-stage light-gas gun of the University of Kent at Canterbury. *Measurement Science Technology* 10:41–50.
- Burchell M. J., Creighton J. A., Cole M. J., Mann J., and Kearsley A. T. 2001. Capture of particles in hypervelocity impacts in aerogel. *Meteoritics & Planetary Science* 36:209–221.
- Burchell M. J., Creighton J. A., and Kearsley A. T. 2004. Identification of organic particles via Raman techniques after capture in hypervelocity impacts on aerogel. *Journal of Raman Spectroscopy* 35:249–253.

- Burchell M. J., Graham G., and Kearsley A. 2006a. Cosmic dust collection in aerogel. *Annual Review of Earth and Planetary Science* 34:385–418.
- Burchell M. J., Mann J., Creighton J. A., Kearsley A. T., Graham G., and Franchi I. A. 2006b. Identification of minerals and meteoritic materials via Raman techniques after capture in hypervelocity impacts on aerogel. *Meteoritics & Planetary Science* 41:217–232.
- Burchell M. J., Fairey S. A. J., Wozniakiewicz P., Brownlee D. E., Hörz F., Kearsley A. T., See T. H., Tsou P., Westphal A., Green S. F., Trigo-Rodríguez J. M., and Domínguez G. 2008. Characteristics of cometary dust tracks in Stardust aerogel and laboratory calibrations. *Meteoritics & Planetary Science* 43:23–40.
- Burchell M. J., Foster N. J., Ormond-Prout J., Dupin D., and Armes S. P. 2009. Extent of thermal ablation suffered by model organic microparticles during aerogel capture at hypervelocities. *Meteoritics & Planetary Science* 44:1407–1420.
- Changela H. G., Bridges J. C., and Gurman S. J. 2012. Extended X-ray absorption fine structure (EXAFS) in Stardust tracks: Constraining the origin of ferric iron-bearing minerals. *Geochimica et Cosmochimica Acta* 98:282–294.
- Chaumard N., Devouard B., Zanda B., and Ferrière L. 2009. The link between CV and CK carbonaceous chondrites based on parent body processes (abstract #5206). 72nd Annual Meteoritical Society Meeting.
- Choi B.-G., McKeegan K. D., Leshin L. A., and Wasson J. T. 1997. Origin of magnetite in oxidised CV chondrites: In situ measurement of oxygen isotope compositions of Allende magnetite and olivine. *Earth and Planetary Science Letters* 146:337–349.
- Christiansen E. L. and Friesen L. 1997. Penetration equations for thermal protection materials. *International Journal of Impact Engineering* 20:153–164.
- Ciesla F. J. 2011. Residence times of particles in diffusive protoplanetary disk environments. II. Radial motions and applications to dust annealing. *The Astrophysical Journal* 740:9.
- De Faria D. L. A., Venâncio Silva S., and de Oliveira M. T. 1997. Raman microspectroscopy of some iron oxides and oxyhydroxides. *Journal of Raman Spectroscopy* 28:873–878.
- De Gregorio B. T., Stroud R. M., Nittler L. R., and Kilcoyne A. L. D. 2015. Evidence for reduced carbon-rich regions in the solar nebula from an unusual cometary dust particle (abstract #2625). 46th Lunar and Planetary Science Conference. CD-ROM.
- Dehn J. 1987. A unified theory of penetration. *International Journal of Impact Engineering* 5:239–248.
- Delhez R., deKeijser T. H., Langford J. I., Louër D., Mittemeijer E. J., and Sonneveld E. J. 1993. Crystal imperfection broadening and peak shape in the Rietveld Method. In *The Rietveld method*, edited by Young R. A. IUCr Monographs in Crystallography, vol. 5. New York: Oxford University Press Inc. pp. 132–166.
- Downs R. T. and Hall-Wallace M. 2003. The American Mineralogist crystal structure database. *American Mineralogist* 88:247–250.
- Floss C., Stadermann F. J., Kearsley A. T., Burchell M. J., and Ong W. J. 2013. The abundance of presolar grains in Comet 81P/Wild 2. *The Astrophysical Journal* 763:140–150.
- Foster N., Wozniakiewicz P. J., Price M. C., Kearsley A. T., and Burchell M. J. 2013. Identification by Raman spectroscopy of Mg–Fe content of olivine samples after impact at 6 km s⁻¹ onto aluminium foil and aerogel: In the laboratory and in Wild-2 cometary samples. *Geochimica et Cosmochimica Acta* 121:1–14.
- Fujiya W., Sugiura N., Sano Y., and Hiyagon H. 2013. Mn–Cr ages of dolomites in CI chondrites and the Tagish Lake ungrouped carbonaceous chondrite. *Earth and Planetary Science Letters* 362:130–142.
- Ghosh A. and McSween H. Y. 1998. A thermal model for the differentiation of Asteroid 4 Vesta, based on radiogenic heating. *Icarus* 134:187–206.
- Gooding J. L. 1981. Mineralogical aspects of terrestrial weathering effects in chondrites from Allan Hills, Antarctica. Proceedings, 12th Lunar and Planetary Science Conference. pp. 1105–1122.
- Gooding J. L. 1986. Weathering of stony meteorites in Antarctica. In *International Workshop on Antarctic Meteorites*, edited by Annestad J. O., Schultz L. and Waenke H. Houston, Texas: Lunar and Planetary Institute. pp. 48–54.
- Graham A. L., Christophe Michel-Levy M., Danon J., and Easton A. J. 1988. The Tuxtuac, Mexico, meteorite, an LL5 chondrite fall. *Meteoritics* 23:321–323.
- Greenberg J. M. 1982. What are comets made of? A model based on interstellar dust. In *Comets*, edited by Wilkening L. L. Tucson, Arizona: The University of Arizona Press. pp. 131–163.
- Haavik C., Stolen S., Fjellvag H., Hanfland M., and Hausermann D. 2000. Equation of state of magnetite and its high-pressure modification: Thermodynamics of the Fe–O system at high pressure. *American Mineralogist* 85:514–523.
- Haggerty S. E. and Baker I. 1967. The alteration of olivine in basaltic and associated lavas. Part I: High temperature alteration. *Contributions to Mineralogy and Petrology* 16:233–257.
- Hanesch M. 2009. Raman spectroscopy of iron oxides and (oxy)hydroxides at low laser power and possible applications in environmental magnetic studies. *Geophysical Journal International* 177:941–948.
- Harju E. R., Rubin A. E., Ahn I., Choi B.-G., Ziegler K., and Wasson J. T. 2014. Progressive aqueous alteration of CR carbonaceous chondrites. *Geochimica et Cosmochimica Acta* 139:267–292.
- Hezel D. C., Russell S. S., Ross A. J., and Kearsley A. T. 2008. Modal abundances of CAIs: Implications for bulk chondrite element abundances and fractionations. *Meteoritics & Planetary Science* 43:1879–1894.
- Hibbert R. and Price M. C. 2014. Characterisation of Raman spectra of high purity olivine as a function of temperature and shock history: Preparation for ExoMars (abstract #1350). 45th Lunar and Planetary Science Conference. CD-ROM.
- Hibbert R., Price M. C., Burchell M. J., and Cole M. J. 2014. Characterisation of Raman spectra of high purity olivine as a function of temperature and shock history (abstract #EPSC2014-295). European Planetary Science Congress 2014.
- Hibbert R., Price M. C., Kinnear T. M., Cole M. J., and Burchell M. J. 2015. The effects of shock pressure on the Raman spectrum of high purity quartz crystals (abstract #1848). 46th Lunar and Planetary Science Conference. CD-ROM.

- Hicks L. J., Bridges J. C., and Gurman S. J. 2014. Ferric saponite and serpentine in the nakhlite martian meteorites. *Geochimica et Cosmochimica Acta* 136:194–210.
- Hong Y. and Fegley B. Jr. 1998. Experimental studies of magnetite formation in the solar nebula. *Meteoritics & Planetary Science* 33:1101–1112.
- Hörz F., Bastien R., Borg J., Bradley J. P., Bridges J. C., Brownlee D. E., Burchell M. J., Chi M., Cintala M. J., Dai Z. R., Djouadi Z., Domínguez G., Economou T. E., Fairey S. A. J., Floss C., Franchi I. A., Graham G. A., Green S. F., Heck P., Hoppe P., Huth J., Ishii H., Kearsley A. T., Kissel J., Leitner J., Leroux H., Marhas K., Messenger K., Schwandt C. S., See T. H., Snead C., Stadermann F. J., Stephan T., Stroud R., Teslich N., Trigo-Rodríguez J. M., Tuzzolino A. J., Troadec D., Tsou P., Warren J., Westphal A., Wozniakiewicz P., Wright I., and Zinner E. 2006. Impact features on Stardust: Implications for Comet 81P/Wild 2 dust. *Science* 314:1716–1719.
- Howard K. T., Benedix G. K., Bland P. A., and Cressey G. 2011a. Modal mineralogy of CM chondrites by X-ray diffraction (PSD-XRD): Part 2. Degree, nature and settings of aqueous alteration. *Geochimica et Cosmochimica Acta* 75:2735–2751.
- Howard K. T., Benedix G. K., Bland P. A., and Schrader D. L. 2011b. Modal mineralogy of CR chondrites by PSD-XRD: Abundance of amorphous Fe-silicate (abstract #5256). 74th Annual Meteoritical Society Meeting.
- Hughes A. L. H. and Armitage P. J. 2010. Particle transport in evolving protoplanetary disks: Implications for results from Stardust. *The Astrophysical Journal* 719:1633–1653.
- Hutchison R. 2004. *Meteorites: A petrologic, chemical and isotopic synthesis*. Cambridge: University of Cambridge Press. 506 p.
- Hutchison R., Alexander C. M. O'D., and Barber D. J. 1987. The Semarkona meteorite: First recorded occurrence of smectite in an ordinary chondrite, and its implications. *Geochimica et Cosmochimica Acta* 51:1875–1882.
- ICDD. 2015. *PDF-4/Minerals 2015 (Database)*. Newtown Square, Pennsylvania: International Centre for Diffraction Data.
- Ishii H. A., Bradley J. P., Dai Z. R., Chi M., Kearsley A. T., Burchell M. J., Browning N. D., and Molster F. 2008. Comparison of Comet 81P/Wild 2 dust with interplanetary dust from comets. *Science* 319:447–450.
- Joswiak D. J., Brownlee D. E., Matrajt G., Westphal A. J., and Snead C. J. 2009. Kosmochloric Ca-rich pyroxenes and FeO-rich olivines (Kool grains) and associated phases in Stardust tracks and chondritic porous interplanetary dust particles: Possible precursors to FeO-rich type II chondrules in ordinary chondrites. *Meteoritics & Planetary Science* 44:1561–1588.
- Joswiak D. J., Nakashima D., Brownlee D. E., Matrajt G., Ushikubo T., Kita N. T., Messenger S., and Ito M. 2014. Terminal particle from Stardust track 130: Possible Al-rich chondrule fragment from comet Wild 2. *Geochimica et Cosmochimica Acta* 144:277–298.
- Kearsley A. T., Burchell M. J., Price M. C., Cole M. J., Wozniakiewicz P. J., Ishii H. A., Bradley J. P., Fries M., and Foster N. J. 2012. Experimental impact features in Stardust aerogel: How track morphology reflects particle structure, composition, and density. *Meteoritics & Planetary Science* 47:737–762.
- Keller L. P. 1998. A transmission electron microscope study of iron-nickel carbides in the matrix of the Semarkona unequilibrated ordinary chondrite. *Meteoritics & Planetary Science* 33:913–919.
- Kerridge J. F. 1970. Some observations on the nature of magnetite in the Orgueil meteorite. *Earth and Planetary Science Letters* 9:299–306.
- Kerridge J. F., Mackay A. L., and Boynton W. V. 1979. Magnetite in CI carbonaceous meteorites: Origin by aqueous activity on a planetesimal surface. *Science* 205:395–397.
- King T. V. V. and King E. A. 1981. Accretionary dark rims in unequilibrated chondrites. *Icarus* 48:460–472.
- King A. J., Schofield P. F., Howard K. T., and Russell S. S. 2015. Modal mineralogy of CI and CI-like chondrites by X-ray diffraction. *Geochimica et Cosmochimica Acta* 165:148–160.
- Kraft S., Stümpel J., Becker P., and Kuetgens U. 1996. High resolution X-ray absorption spectroscopy with absolute energy calibration for the determination of absorption edge energies. *Review of Scientific Instruments* 67:681–687.
- Krot A. N., Scott E. R. D., and Zolensky M. E. 1995. Mineralogical and chemical modification of components in CV3 chondrites: Nebular or asteroidal processing? *Meteoritics* 30:748–775.
- Krot A. N., Petaev M. I., Scott E. R. D., Choi B.-G., Zolensky M. E., and Keil K. 1998a. Progressive alteration in CV3 chondrites: More evidence for asteroidal alteration. *Meteoritics & Planetary Science* 33:1065–1085.
- Krot A. N., Petaev M. I., Zolensky M. E., Keil K., Scott E. R. D., and Nakamura K. 1998b. Secondary calcium-iron-rich minerals in the Bali-like and Allende-like oxidised CV3 chondrites and Allende dark inclusions. *Meteoritics & Planetary Science* 33:623–645.
- Krot A. N., Brearley A. J., Petaev M. I., Kallemeyn G. W., Sears D. W. G., Benoit P. H., Hutcheon I. D., Zolensky M. E., and Keil K. 2000. Evidence for low-temperature growth of fayalite and hedenbergite in MacAlpine Hills 88107, an ungrouped carbonaceous chondrite related to the CM-CO clan. *Meteoritics & Planetary Science* 35:1365–1386.
- Lafuante B., Downs R. T., Yang H., and Stone N. 2015. The power of databases: The RRUFF project. In *Highlights in Mineralogical Crystallography*, edited by Armbruster T. and Danisi R. M. Berlin, Germany: De Gruyter. pp. 1–30.
- Le Guillou C., Changela H. G., and Brearley A. J. 2015. Widespread oxidised and hydrated amorphous silicates in CR chondrites matrices: Implications for alteration conditions and H₂ degassing of asteroids. *Earth and Planetary Science Letters* 420:162–173.
- Leroux H. 2012. Fine-grained material of 81P/Wild 2 in interaction with the Stardust aerogel. *Meteoritics & Planetary Science* 47:613–622.
- Marrocchi Y., Chaussidon M., Piani L., and Libourel G. 2016. Early scattering of the solar protoplanetary disk recorded in meteoritic chondrules. *Science Advances* 2: e1601001.
- Mason B., and Wiik H. B. 1962. *The Renazzo meteorite*. American Museum Novitates #2106. New York: American Museum of Natural History. 11 p.
- Matzel J. E. P., Ishii H. A., Joswiak D., Hutcheon I. D., Bradley J. P., Brownlee D., Weber P. K., Teslich N., Matrajt G., McKeegan K. D., and MacPherson G. J. 2010. Constraints on the formation age of cometary

- material from the NASA Stardust mission. *Science* 328:483–486.
- McSween H. Y. and Taylor L. A. 1978. Metamorphic effects in experimentally heated Krymka (L3) chondrite. Proceedings, 9th Lunar and Planetary Science Conference. pp. 1437–1447.
- McSween H. Y. and Treiman A. H. 1998. Martian meteorites. In *Planetary materials*, edited by Papike J. J. Reviews in Mineralogy, vol. 36. Washington, D.C.: Mineralogical Society of America. pp. 6.1–6.53.
- Merk R., Breuer D., and Spohn T. 2002. Numerical modeling of ^{26}Al -induced radioactive melting of asteroids considering accretion. *Icarus* 159:183–191.
- Mittlefehldt D. W., McCoy T. J., Goodrich C. A., and Kracher A. 1998. Non-chondritic meteorites from asteroidal bodies. In *Planetary materials*, edited by Papike J. J., Reviews in Mineralogy, vol. 36, Washington, D.C.: Mineralogical Society of America. pp. 4.1–4.195.
- Miyamoto M., Fujii N., and Takeda H. 1981. Ordinary chondrite parent body: An internal heating model. Proceedings, 12th Lunar and Planetary Science Conference. pp. 1145–1152.
- Mosselmans J. F. W., Quinn P. D., Dent A. J., Cavill S. A., Moreno S. D., Peach A., Leicester P. J., Keylock S. J., Gregory S. R., Atkinson K. D., and Rosell J. R. 2009. I18—The microfocuss spectroscopy beamline at the Diamond Light Source. *Journal of Synchrotron Radiation* 16:818–824.
- Nakamura T., Noguchi T., Tsuchiyama A., Ushikubo T., Kita N. T., Valley J. W., Zolensky M. E., Kakazu Y., Sakamoto K., Mashio E., Uesugi K., and Nakano T. 2008. Chondrulelike objects in short-period Comet 81P/Wild 2. *Science* 321:1664–1667.
- Nayakshin S., Cha S.-H., and Bridges J. C. 2011. The tidal downsizing hypothesis for planet formation and the composition of solar system comets. *Monthly Notices of the Royal Astronomical Society Letters* 416:L50–L54.
- Noguchi T., Nakamura T., Okudaira K., Yano H., Sugita S., and Burchell M. J. 2007. Thermal alteration of hydrated minerals during hypervelocity capture to silica aerogel at the flyby speed of Stardust. *Meteoritics & Planetary Science* 42:357–372.
- O'Driscoll B., Clay P. L., Cawthorn P. L., Lenaz D., Adetunji J., and Kronz A. 2014. Trevorite: Ni-rich spinel formed by metasomatism and desulfurization processes at Bon Accord, South Africa? *Mineralogical Magazine* 78:145–163.
- Ogliore R. C., Huss G. R., Nagashima K., Butterworth A. L., Gainsforth Z., Stodolna J., Westphal A. J., Joswiak D., and Tyliczszak T. 2012. Incorporation of a late-forming chondrule into Comet Wild 2. *The Astrophysical Journal Letters* 745:L19.
- Pecharroman C., Gonzalez-Carreno T., and Iglesias J. E. 1995. The infrared dielectric properties of maghemite, gamma- Fe_2O_3 , from reflectance measurement on pressed powders. *Physics and Chemistry of Minerals* 22:21–29.
- Popp J., Tarcea N., Kiefer W., Hilchenbach M., Thomas N., Stuffer T., Hofer S., Stöffler D., and Greshake A. 2002. The effect of surface texture on the mineralogical analysis of chondritic meteorites using Raman spectroscopy. *Planetary and Space Science* 50:865–870.
- Price M. C., Wozniakiewicz P. J., Bridges J. C., Hicks L. J., and Burchell M. J. 2012. Raman analyses of Stardust terminal grain in Track 170 (abstract #EPSC2012-333). European Planetary Science Congress 2012.
- Price M. C., Bridges J. C., Wozniakiewicz P. J., and Hicks L. J. 2014. Results from Raman analyses of thirty-six Stardust cometary grains from tracks 170, 176, 177, 178 (abstract #1252). 45th Lunar and Planetary Science Conference. CD-ROM.
- Roy M. and Gurman S. J. 2001. An investigation of the use of the Hedin-Lundqvist exchange and correlation potential in EXAFS data analysis. *Journal of Synchrotron Radiation* 8:1095–1102.
- Sanderson D. D. 1974. Spatial distribution and origin of magnetite in an intrusive igneous mass. *Geological Society of America Bulletin* 85:1183–1188.
- Semenenko V. P., Jessberger E. K., Chaussidon M., Weber I., Stephan T., and Wies C. 2005. Carbonaceous xenoliths in the Krymka LL3.1 chondrite: Mysteries and established facts. *Geochimica et Cosmochimica Acta* 69:2165–2182.
- Simon S. B., Joswiak D. J., Ishii H. A., Bradley J. P., Chi M., Grossman L., Aléon J., Brownlee D. E., Fallon S., Hutcheon I. D., Matrajt G., and McKeegan K. D. 2008. A refractory inclusion returned by Stardust from comet 81P/Wild 2. *Meteoritics & Planetary Science* 43:1861–1877.
- Stodolna J., Jacob D., and Leroux H. 2012a. Mineralogy and petrology of Stardust particles encased in the bulb of track 80: TEM investigation of the Wild 2 fine-grained material. *Geochimica et Cosmochimica Acta* 87:35–50.
- Stodolna J., Jacob D., Leroux H., and Burchell M. J. 2012b. Microstructure modifications of silicates induced by the collection in aerogel: Experimental approach and comparison with Stardust results. *Meteoritics & Planetary Science* 47:696–707.
- Tomić S., Searle B. G., Wander A., Harrison N. M., Dent A. J., Mosselmans J. F. W., and Inglesfield J. E. 2004. New Tools for the Analysis of EXAFS: The DL_EXCURV Package. CCLRC Technical Report DL-TR-2005-001.
- Trigo-Rodríguez J. M., Domínguez G., Burchell M. J., Hörz F., and Llorca J. 2008. Bulbous tracks arising from hypervelocity capture in aerogel. *Meteoritics & Planetary Science* 43:75–86.
- Uesugi M., Uesugi K., Takeuchi A., Suzuki Y., Hoshino M., and Tsuchiyama A. 2013. Three-dimensional observation of carbonaceous chondrites by synchrotron radiation X-ray CT—Quantitative analysis and developments for the future sample return missions. *Geochimica et Cosmochimica Acta* 116:17–32.
- Wechsler B. A., Lindsley D. H., and Prewitt C. T. 1984. Crystal structure and cation distribution in titanomagnetites ($\text{Fe}_{3-x}\text{Ti}_x\text{O}_4$). *American Mineralogist* 69:754–770.
- Weisberg M. K., McCoy T. J., and Krot A. N. 2006. Systematics and evaluation of meteorite classification. *Meteorites and the early solar system II*, edited by Lauretta D. S. and McSween H. Y. Jr. Tucson, Arizona: The University of Arizona Press. pp. 19–52.
- Westphal A. J., Snead C., Borg J., Quirico E., Raynal P.-I., Zolensky M. E., Ferrini G., Colangeli L., and Palumbo P. 2002. Small hypervelocity particles captured in aerogel collectors: Location, extraction, handling and storage. *Meteoritics & Planetary Science* 37:855–865.
- Westphal A. J., Snead C., Butterworth A., Graham G. A., Bradley J. P., Bajt S., Grant P. G., Bench G., Brennan S., and Pianetta P. 2004. Aerogel keystones: Extraction of

- complete hypervelocity impact events from aerogel collectors. *Meteoritics & Planetary Science* 39:1375–1386.
- Westphal A. J., Fakra S. C., Gainsforth Z., Marcus M. A., Ogliore R. C., and Butterworth A. L. 2009. Mixing fraction of inner solar system material in Comet 81P/Wild 2. *The Astronomical Journal* 694:18–28.
- Westphal A. J., Bridges J. C., Brownlee D. E., Butterworth A. L., De Gregorio B. T., Dominguez G., Gainsforth Z., Flynn G. J., Ishii H. A., Joswiak D., Nittler L. R., Ogliore R. C., Pepin R. O., Palma R., Stephan T., and Zolensky M. E. 2017. The future of Stardust science. *Meteoritics & Planetary Science* doi:10.1111/maps.12893
- Wilke M., Farges F., Petit P.-E., Brown G. E. Jr., and Martin F. 2001. Oxidation state and coordination of Fe in minerals: An Fe K-XANES spectroscopic study. *American Mineralogist* 86:714–730.
- Wozniakiewicz P. J., Ishii H. A., Kearsley A. T., Bradley J. P., Price M. C., Burchell M. J., Teslich N., and Cole M. J. 2015. The survivability of phyllosilicates and carbonates impacting Stardust Al foils: Facilitating the search for cometary water. *Meteoritics & Planetary Science* 50:2003–2023.
- Yu-Qui W., Erkang W., and Wen-lan Z. 1997. A comparison between cosmic spinel and terrestrial spinel. *Acta Metallurgica Sinica* 3:23–30.
- Zolensky M. E., Zega T. J., Yano H., Wirick S., Westphal A. J., Weisberg M. K., Weber I., Warren J. L., Velbel M. A., Tsuchiyama A., Tsou P., Toppani A., Tomioka N., Tomeoka K., Teslich N., Taheri M., Susini J., Stroud R., Stephan T., Stadermann F. J., Snead C. J., Simon S., Simionovici A., See T. H., Robert F., Rietmeijer F. J. M., Rao W., Perronnet M., Papanastassiou D. A., Okudaira K., Ohsumi K., Ohnishi I., Nakamura-Messenger K., Nakamura T., Mostefaoui S., Mikouchi T., Meibom A., Matrajt G., Marcus M. A., Leroux H., Lemelle L., Le L., Lanzirotti A., Langenhorst F., Krot A. N., Keller L. P., Kearsley A. T., Joswiak D., Jacob D., Ishii H., Harvey R., Hagiya K., Grossman L., Grossman J. N., Graham G. A., Gounelle M., Gillet P., Genge M. J., Flynn G., Ferroir T., Fallon S., Ebel D. S., Dai Z. R., Cordier P., Clark B., Chi M., Butterworth A. L., Brownlee D. E., Bridges J. C., Brennan S., Brearley A., Bradley J. P., Bleuet P., Bland P. A., and Bastien R. 2006. Mineralogy and petrology of Comet 81P/Wild 2 nucleus samples. *Science* 314:1735–1739.
-